# Critical Technologies Maturation & Evaluation of Pathfinder Architecture for Habitable Worlds Observatory

**Alain Carrier,[a,*] Alison Nordt,[a] John Conklin,[c] Roger Glaese,[b] Scott M. Aronson,[c] Michael S. Jacoby,[f] Daniel Kaplan,[d] Jeffrey R. Olson,[a] Liz Osborne,[a] James D. Phillips,[d] Robert Reasenberg,[c,e] Thomas J. Roberts,[d] Kiarash Tajdaran,[a] Jacob Wirth,[a] Rodrigo Zeledon[a]**

[a] Lockheed Martin Advanced Technology Center, 3251 Hanover St, Palo Alto, CA, USA
[b] Moog, 2581 Leghorn Street, Mountain View, CA, USA
[c] University Of Florida, Precision Space Systems Laboratory, Department of Mechanical and Aerospace Engineering, Gainesville, FL, USA
[d] Illinois Institute Of Technology, Department of Physics, Chicago, IL, USA
[e] Eureka Scientific, Inc., Oakland, CA, USA
[f] Chicks In Space, Inc., 339 Alameda de las Pulgas, Redwood City, CA, USA

**Abstract.** In 2021, following promising feasibility studies led by NASA, the National Academies in the Decadal Survey on Astronomy and Astrophysics officially recommended a flagship mission to search for the existence of life outside of our solar system. In response, NASA in partnership with the astrophysics community and with support from industry is currently performing architecture studies and advancing critical technologies for the Habitable Worlds Observatory (HWO), a next generation large space observatory capable of directly imaging and characterizing Earth-like exo-planets in the habitable zone of nearby stars. HWO uses a coronagraph to block the light of the parent star and demands unprecedented levels of wavefront stability on the order of 10 picometers over long time scales to achieve the raw contrast ratio of better than $10^{-10}$ and the contrast stability of $10^{-12}$ necessary for direct exo-Earth imaging.

In this article, we report on Lockheed Martin team's progress advancing four critical technologies for HWO covering vibration isolation and precision pointing systems, picometer-class metrology, structural damping augmentation, and cryogenic detector cooling. We also report on our evaluation of the dynamic line-of-sight and dynamic wavefront error stability achieved during science observation and following large angle slews using Lockheed Martin's Disturbance Free Payload (DFP) system for vibration isolation from the host spacecraft to the telescope on a pathfinder observatory architecture developed by NASA and its partners called Exploratory Analytical Case 1. The optical telescope assembly in that case consists of an off-axis 6-meter inscribed-diameter segmented primary mirror with 19 segments and an unobscured telescope.

Our approach to achieving the requisite dynamic wavefront stability with DFP consists in flying the optical telescope assembly and the host spacecraft in close formation. In that architecture, the telescope is mechanically disconnected from the spacecraft aside from harnesses bridging that interface, thereby providing superior levels of vibration isolation. DFP enables high science observation efficiencies with little-to-no downtime following slews and enables tight telescope attitude control at ~0.6-Hz bandwidth.

We discuss our study findings to-date and the implications for the design of the observatory and its active wavefront sensing and control system.

**Keywords**: Habitable Worlds Observatory, space segmented telescopes, ultra-stability, dynamic wavefront error, vibration isolation, precision pointing, Disturbance Free Payload, picometer metrology, heterodyne laser gauge, tracking frequency gauge, structural damping augmentation, cryogenic detector cooling.

# 1 Introduction and Study Objectives

In the next two decades, NASA envisions a large space-based telescope that will perform unprecedented astronomy focused on the direct detection and characterization of Earth-like exoplanets[1,2] Recent advances in optical coronagraphs have enabled this mission, but the technology imposes unprecedented requirements on telescope dimensional stability, optical system alignment sensing and control, and vibration isolation. Optical coronagraphs enable detection and characterization of exoplanets in the close angular proximity of their parent star by effectively removing the central core of the stellar Point Spread Function, leaving an annular “dark hole,” whose inner and outer angular limits are defined by the telescope and coronagraph instrument performance. A key performance metric of coronagraphs is defined by the contrast ratio that measures the effectiveness of the coronagraph in suppressing the starlight near the planet. For the system architectures being considered by NASA, raw contrast ratios on the order of $10^{-10}$ are required, and this contrast performance level must be sustained over long time intervals between wavefront error (WFE) sensing and control updates. Over these intervals, contrast stability is degraded by uncompensated optical WFE due to dynamic vibration of telescope optics arising from spacecraft exported vibrations and thermal-induced structural deformations.

NASA HWO Technology Maturation Project Office (HTMPO) reported on HWO’s critical technologies and development needs in Ref. 3. Our long-term objectives include advancing the following four critical technologies on that list to Technology Readiness Level 5 in preparation for Mission Concept Review (MCR) in 2029: “Telescope Sensing & Control” categorized as Threshold and prioritized as Critical, “Low-Vibration & Pointing Control Systems” categorized as Threshold and prioritized as Long Term, “Ultra-Stable Structures” categorized as Threshold and prioritized as Urgent, and “Cryogenic/Superconducting Detectors” categorized as Enhanced and prioritized as Critical. Concurrently, our objective is to advance integrated modeling tools to explore the observatory architecture trade space and project the observatory end-to-end performance. In this article, we present an application of those tools to project HWO’s dynamic line-of-sight and dynamic wavefront performance on NASA Exploratory Analytical Case 1 (EAC1) pathfinder architecture as a use-case.

This article is organized as follows. In Section 2, we provide an overview of NASA EAC1 use-case used in our integrated modeling analyses and our metrology configuration studies. Section 3 focuses on critical technology maturation for the mission. We provide an overview of the Disturbance Free Payload system for Optical-Telescope-Assembly (OTA) inertial stabilization and precision pointing and discuss our approach to tailoring that system to EAC1. We report on our progress on advancing picometer optical metrology gauges needed to sense the OTA deformations and control the dimensional stability of that assembly. That progress includes a laboratory experiment conducted by differencing the outputs from two Tracking Frequency Gauges on a common-path test-bed in air: the displacement measurement stability achieved is <3 pm over correlation times ranging from 3 msec to 2.8-hours in that configuration. We report on effective means leveraging the picometer actuators needed for positioning the telescope optical elements to actively augment the structural damping of the OTA without introducing additional hardware and without impacting the thermal-dimensional stability of that assembly. Lastly, we report on our progress devising cryogenic cooling solutions to accommodate cryogenic/superconducting detectors and thereby potentially enhance planet yield by 30%.[4] Section 4 reports on the results of our integrating modeling studies on EAC1 and demonstrates the slew agility, dynamic line-of-sight stability, and dynamic wavefront stability benefits of the Disturbance Free Payload system. That section concludes with our projected bottoms up dynamic line-of-sight and dynamic wavefront error budgets with DFP. Section 5 summarizes our EAC1 evaluation findings and derived observatory recommendations. Section 6 concludes with next steps and future work.

## 2 NASA Exploratory Analytical Case 1 Pathfinder Architecture Use-Case

Exploratory Analytical Case 1 (EAC1) is one of three exploratory analytical cases being studied by NASA and its partners, and Industry to exercise the integrated modeling tools and to raise the

Concept Maturity Level for the Habitable Worlds Observatory. Those EACs are not intended to be point designs. As shown in Figure 1, the observatory is composed of a spacecraft and a payload interfacing through a vibration isolation system. The optical telescope assembly in this case consists of an off-axis 6-meter inscribed-diameter segmented primary mirror with 19 segments and an unobscured telescope. The optical telescope is surrounded by a baffle for micrometeoroids protection.

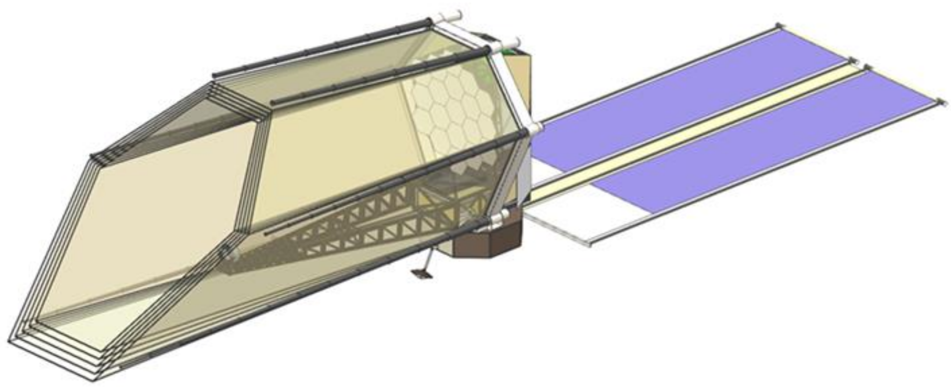

**Fig. 1** (Credit NASA): Exploratory Analytical Case 1 Overview.

## 3 Critical Technologies for Ultra-Stable Telescope

### *3.1 Disturbance Free Payload System for Telescope Vibration Isolation and Precision Pointing*

For vibration isolation of the observatory payload from the host spacecraft, we baseline our Disturbance Free Payload (DFP) system to fly the payload (optical telescope) and the host spacecraft in close formation. In that architecture, the telescope is mechanically disconnected from the spacecraft aside from electrical and digital data harnesses bridging that interface, thereby providing superior levels of vibration isolation. The Disturbance Free Payload system addresses the needs for "Low-Vibration & Pointing Control Systems", a technology categorized as Threshold and prioritized as Long Term for HWO.[3,5]

#### *3.1.1 Disturbance free payload overview and heritage*

We demonstrated the DFP system vibration isolation, payload precision pointing, and slew functionalities extensively[6-9] on multiple 2-D and 3-D laboratory testbeds (some shown in Figure 2) and achieved 68-dB of vibration isolation from 1-Hz to 100 Hz on 3-D emulators replicating the dynamics of large observatory precursors to James Webb Space Telescope (JWST) at reduced scale. That technology is currently at Technology Readiness Level 4.

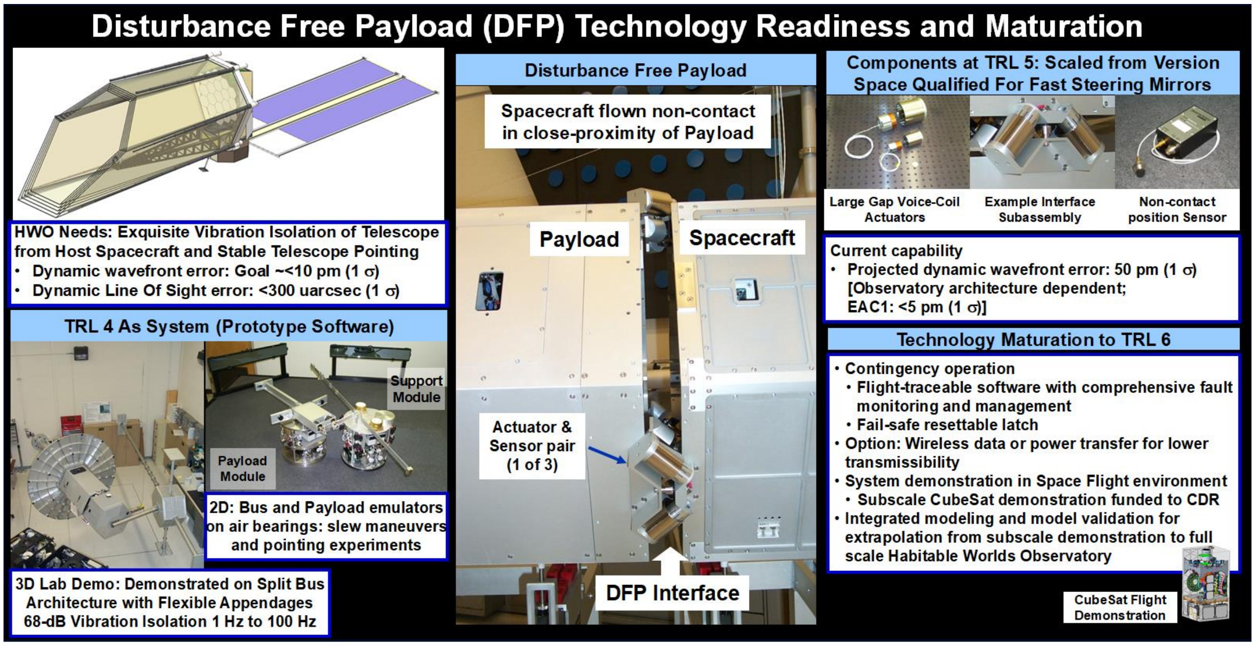




**Fig. 2** DFP Demonstrated Superior Levels of Vibration Isolation on 3D Emulators Relevant to HWO Replicating the Dynamics of Large Observatories at Reduced Scale.

In the configuration used in this work, the Disturbance Free Payload system has 3 main control functions: (1) Payload inertial attitude pointing, (2) relative position control between spacecraft and payload, (3) spacecraft attitude control relative to payload. That configuration is a variant of the so-called pure DFP configuration depicted in Figure 3, which does not use the spacecraft thrusters for relative position control.

- Payload inertial attitude pointing as its name implies is intended to maintain the optical telescope pointed towards its target. That control function is achieved using the DFP non-contact voice-coil actuators for actuation and the payload attitude sensors (such as star trackers, gyroscopes, and guiders) for attitude determination. DFP applies torques to the payload using its non-contact voice-coil actuators to execute the attitude corrections requested by the payload; DFP uses the spacecraft as reaction structure.
- Relative position control is intended to maintain DFP within its +/-10 mm operational range; that control does not have to be very precise; it only needs to be good enough to maintain DFP within its operational range. That control function is achieved using the DFP non-contact voice-coil actuators for actuation and non-contact position sensors for monitoring the position of the spacecraft relative to the payload. The actuation forces are combined so that ideally the resultant

torque about the payload center of mass is null to avoid perturbing the payload attitude in the process. In the so-called pure DFP configuration, that control function would be achieved using thrusters to reposition the spacecraft relative to the payload instead of the voice-coil actuators: that is an acceptable compromise in applications where what matters is the payload inertial attitude or target pointing not the payload position.

- Relative attitude control is also intended to maintain DFP within its operational range and again that control does not have to be very precise; it only needs to be good enough to maintain DFP within its operational range. That control function is achieved using the spacecraft reaction wheels for actuation and the DFP non-contact position sensors for monitoring the attitude of the spacecraft relative to the payload. The relative attitude control is like drag-free satellite operation. It is worth pointing out and emphasizing that DFP does not use its voice-coil actuators for relative attitude control because doing so would affect the payload pointing.

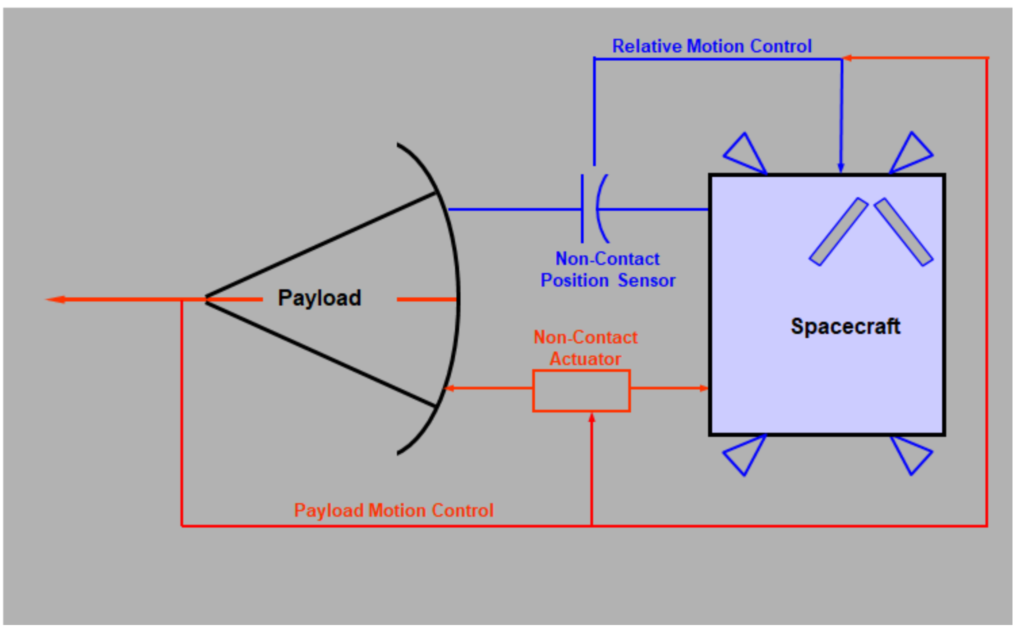


**Fig. 3** The pure DFP control system configuration.

In the so-called pure DFP configuration, DFP would achieve vibration isolation down to DC in the absence of mechanical coupling such as cables at the interface between the spacecraft and the payload and the performance would not be limited by the relative position sensor noise since those sensor signals would not be used to generate any forces or torques applied to the payload. That feature distinguishes DFP from conventional active vibration isolation or cancellation systems.

The relative position and the relative attitude tolerance being loose, we operate those functions at low bandwidth for stability robustness purposes in the presence of appendages low-frequency structural dynamics. How low that bandwidth can be is a trade-off versus the observatory slew agility and the designed-in DFP operational range.

The DFP control logic can be configured so that either the payload, the spacecraft, or DFP acts as the master for coordinating operation. In this work, DFP is designated as the master.

*3.1.2 Voice coil actuator current drive noise mitigation*

VCAs are Lorentz force actuators, generating a force which is proportional to the electrical current through a coil suspended in a fixed magnetic field. Voice Coil Drivers (VCDs) are analog electronics boards that deliver controlled current through the VCAs from an external command. In low-noise applications such as DFP, these drivers use linear current regulators. A current control loop is typically implemented in the analog electronics to cancel the back EMF, which arises in the presence of relative motion between the coil and the magnet, so that the electrical current delivered to the coil is ideally equal to the current requested. The command signal is typically a digital signal converted to an analog voltage using a digital-to-analog converter (DAC).

In previous integrated modeling studies of a DFP architecture for HWO,[10] the VCDs were modeled using the noise characteristics and frequency response for drive electronics typically deployed for precision mechanism control, such as with a Fast-Steering Mirror (FSM). For an HWO application of DFP, the noise performance of VCA drivers can be improved significantly by tuning the heritage VCA drivers for the specific needs of HWO.

Noise performance can be increased in the VCD electronics by either improving the noise characteristics of the DAC, tuning the analog circuit, or changing the bandwidth of the current control loop. All three techniques are explored and simulated to arrive at a VCD design that achieves over 6.5x noise reduction compared with heritage FSM designs.

The noise characteristics of VCDs from three heritage FSM programs were analyzed, and the driver used in a Lockheed Martin (LM) FSM development program called “AIMS-2” was selected as the starting point for tuning the circuit for a DFP implementation on HWO. Two modifications in the circuit reduce the noise by a factor of 2.2x in the 30 Hz – 70 Hz range: the addition of low-noise Analog Devices OP27 amplifiers to the error and current sense stages of the drive electronics, and a change in the resistance of the current sense resistors. These modifications incur a slight 0.1W increase in quiescent power.

Additional reduction in noise can be achieved by lowering the bandwidth of the current control loop. The payload pointing control loop within the DFP system has a bandwidth of approximately 0.58 Hz for HWO's Exploratory Analysis Configuration-1 (EAC-1), so the current control loop bandwidth can be reduced from a starting point of 400 Hz to 6 Hz and still be operating a decade above the payload pointing control loop's bandwidth. Lowering the current control bandwidth has the disadvantage of increasing coupling between spacecraft and payload, due to lower back EMF rejection. Integrated modeling assessments, however, show that the effect on performance metrics from back EMF is relatively small compared to the effect of coupling due to cables across the DFP interface, and well worth the tradeoff for lower VCD noise.[11] Operating the current control loop with a bandwidth of 6 Hz results in another 2.6x reduction in noise compared with the same circuit at 400 Hz bandwidth. Figure 4 shows a comparison of the simulated noise spectral densities and back EMF rejection of the heritage VCD (purple) and the circuit tuned for DFP at three different bandwidths. The 30-Hz-to-70-Hz band is highlighted since that is the frequency band where the payload has significant structural modes, and excitation from the VCD noise would have the largest effect on wavefront error. Table 1 shows the integrated noise results and power consumption of the circuits analyzed.

**Table 1** Simulation Results for Voice Coil Drive Circuits.

| VCD Design | Current Noise, 1Hz-5k Hz (uA) | Current Noise, 30 Hz-70 Hz (uA) | Quiescent Power (W) | Power at Peak Current (W) |
|---|---|---|---|---|
| AIMS-2 | 15.9 | 0.40 | 0.72 | 35.1 |
| **DFP 6 Hz** | **0.52** | **0.06** | **0.76** | **35.2** |
| DFP 160 Hz | 0.43 | 0.16 | 0.76 | 35.2 |
| DFP 400 Hz | 0.60 | 0.17 | 0.76 | 35.2 |

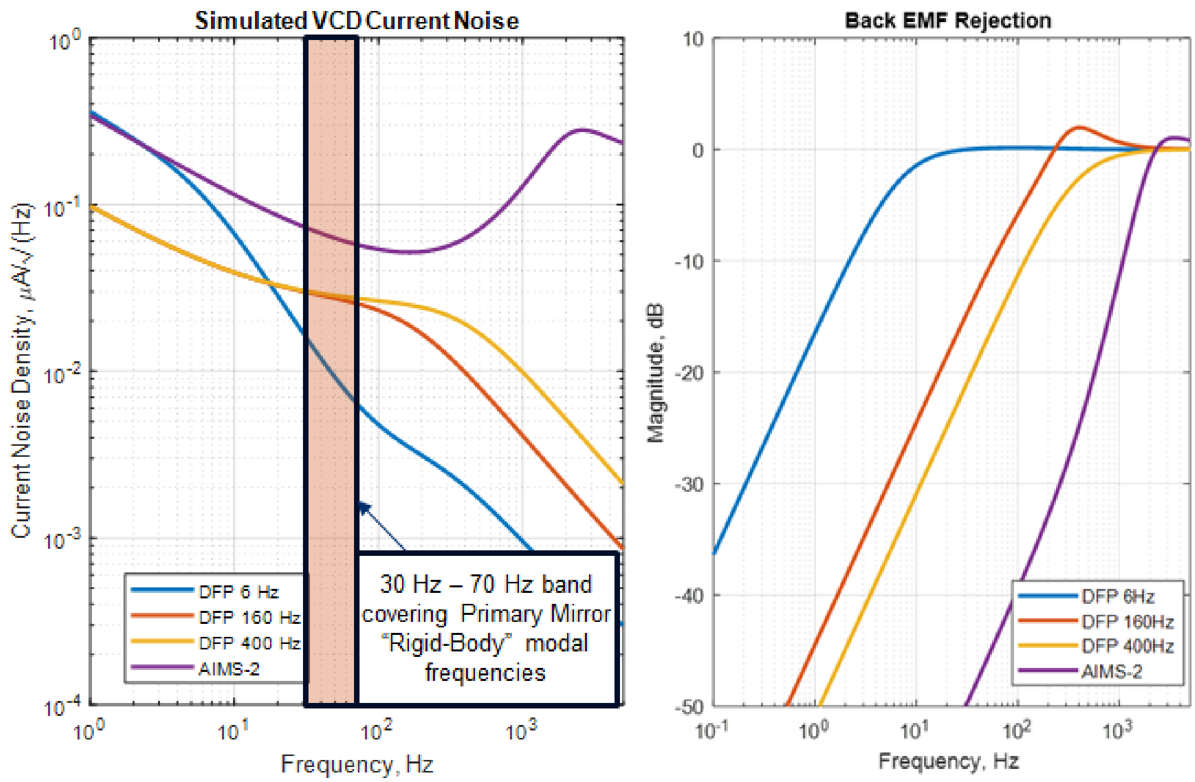


**Fig. 4** Current Noise Density and Back EMF Rejection of Simulated Circuits.

*3.1.3 Harness for electrical power accommodation across vibration isolation system interface*

In the Disturbance Free Payload architecture, the harness bridging the otherwise mechanically non-contact interface between the payload and the spacecraft is the main source of vibration transmissibility. Both the collective stiffness and preset of those harnesses are important considerations for the design of the DFP voice-coil actuators in terms of their force and force range. Sizing the cable harnesses specific to HWO that will bridge that interface for the purpose of transferring electrical power from the host spacecraft to the payload and for the purpose of transferring data between the spacecraft and the payload is work in progress. Our plans include fabricating and characterizing the collective stiffness of a cable harness that is representative for HWO, which can then be used to anchor our integrated modeling studies.

**Table 2** Data Rate and Power Estimates for Payload Components in EAC-1.

| Instrument/Subsystem | Estimated Data Rate (Mb/s) | Power Allocation (W) | Notes |
|---|---|---|---|
| Coronagraph Instrument (CGI) | 713 | 1164.6 | Broadband imager and spectrometer[17,18] |
| High-Resolution Instrument (HRI) | 90.9 | 183.3 | Data rates based on similar readout to WFC3[12,14] |

| | | | |
|---|---|---|---|
| UV Instrument (UVI) | 251.7 | 523.8 | Data rates based on LUMOS/LUVOIR estimates with only far or near UV channel active at a time[14,15] |
| XI (Extra Instrument) | 713 | 582.3 | Assumes data rate equal to CGI, power allocation half of CGI[12] |
| Guiders and IRU | 13.2 | 242.2 | Assumes 2 Fine Guidance Sensors and 1 Inertial Reference Unit[12,16] (see *Note) |
| Optical Telescope Element | | 14000 | Allocation[12] |
| **Total** | **1781.8** | **16696.4** | |

* Note: The EAC1 integrated model described in Section 4 assumes a Hemispherical Resonator Gyro (HRG) identical to that used on the James Webb Space Telescope; known power consumption and data rate for a similar HRG described in Ref. 16 were used as a surrogate.

As shown in Table 2, current projections for EAC1 indicate that the payload may require up to 17,000 Watt at 70V. Given that large amount of electrical power, the stiffness of the communication/data cable will be negligible in comparison to that of the electrical power harness resulting in no worthwhile benefits in considering wireless communication/data transfer. Our preliminary collective cable harness stiffness projections are based on measured cable stiffness data for the Geostationary Lightning Mapper (GLM) and the Advanced Baseline Imager (ABI) power cables that bridge the D-Strut-based vibration isolation system interface between the spacecraft and the isolated Earth Pointing Platform on Geostationary Operational Environmental Satellites (GOES-R).[17] We scaled those measured stiffness values based on relative required electrical power and bus supply voltages between HWO and those two GOES instruments to arrive at the placeholder stiffness values used in this study, namely a linear stiffness of 50 lbf/in and a torsional stiffness of 17.45 lbf-in/deg.

Ultimately, the stiffness of that power cable will depend on specific composition (gauge and number of conductors per wire), number of wires, and layout including service loops: these are all design considerations under the ongoing effort. It would be desirable to configure the cable harnesses so that the center of stiffness of the collective cable harness coincides with the center of mass of the payload, which would minimize the cross-coupling vibration transmissibility from spacecraft linear accelerations to payload angular accelerations: unfortunately, that objective cannot be approached on EAC1 due to the large offset on the order of 3-m between the combined system center of mass and the vibration isolation system interface. It would also be desirable to have the cable harness centrally located on the isolation system interface as opposed to distributed in bundles at the periphery of the isolation system interface to minimize the collective moment stiffness and reduce the forces required of the voice-coil actuators to overcome the moment stiffness of those cables for payload pointing corrections. For a sense of scale, we project that the maximum force required of any given voice-coil actuator to overcome a cable with a moment stiffness of 17.45 lbf-in/deg over the full +/-10-mm actuation range is about 0.21 N in our baseline voice-coil actuator configuration out of a continuous force capability of 5 N.

The cable preset would become a driver on the force required of the voice-coil actuators if one were to attempt operating DFP exactly in the middle of its operational range: any given voice-coil actuator for instance would need to generate up 5.84-N of force out of a continuous force capability of 5-N to overcome a 1-mm preset for a cable with a linear stiffness of 50 lbf/in in our baseline actuator configuration. Simply increasing the voice-coil actuator force capability is not desirable due to the increase in actuation noise for a given dynamic range. A better strategy is to allow operation around the equilibrium condition at a relative pose set point away from the middle of the actuation range: the actuation range being about +/-10-mm in any direction, the preset can be a couple millimeters thereby imposing a relatively easy to achieve preset tolerance through a set-and-forget cable preset adjustment mechanism, if necessary.

**Interface Cable Coupling and Modeling**

Cables have non-linear stiffness and damping characteristics and are notoriously difficult to model. The Disturbance Free Payload control logic itself does not require precise knowledge of either the stiffness or the damping characteristics of the interface cables. That control logic includes cable stiffness cancellation using positive relative position feedback through a first order low-pass filter (effectively implementing a negative spring at low frequencies). We typically set the cancellation ratio to 70% which allows for up to 30% uncertainty in the knowledge of that cable stiffness. That compensation has also the effect of reducing the amplification at resonance down to a Q of 2 to 4 without requiring knowledge of the damping at resonance prior to compensation (even no damping would be acceptable as far as that compensation logic is concerned).

Predicting the vibration transmissibility from spacecraft accelerations to payload accelerations at frequencies significantly above the coupled system resonance on the other hand can require knowledge of the cable damping mechanism depending on the fundamental structural natural frequency of the payload for the following reasons. HWO requires extreme levels of vibration isolation between the Payload and the Spacecraft to achieve its wavefront stability on the order of 10 pm (1 $\sigma$) when reaction-wheels or control-moment-gyros are used for spacecraft attitude control. Prior analyses on LUVOIR projected uncompensated dynamic wavefront errors of 50 pm (1 σ) and identified voice-coil actuator noise and transmissibility due to cable harness damping as two dominant sources of errors limiting the uncompensated dynamic LOS and dynamic wavefront errors stability achievable within the DFP architecture.[18] The lower the fundamental structural natural frequency of the Payload, the higher the susceptibility of the payload dimensional stability to residual exported vibrations. In cases where that fundamental natural frequency is low--it was about 1.5-Hz on LUVOIR-B--, one may need to predict the transmissibility of vibrations from the host spacecraft to the segmented telescope out to several hundred Hertz to evaluate dynamic wavefront stability performance to the requisite levels. Currently, there is a knowledge gap in making such predictions in that the extent to which rate (viscous) damping in harnesses is present and contributes to significant increase in transmissibility at frequencies more than 100 times the "rigid-body" mode frequencies, is not understood. Closing that knowledge gap would require characterizing the regime between position-dependent and rate-dependent damping mechanisms in representative harnesses in subscale demonstration—rate damping being most detrimental to transmissibility at high frequencies. We currently model damping as viscous damping and roll-off that rate damping through a first order low-pass filter with a corner frequency 10 times above the coupled system modal resonances presuming that the damping mechanism in cables is dominantly position-dependent. Closing that knowledge gap becomes less critical if one designs the telescope structure to be relatively stiff, which reduces the susceptibility of that structure to residual dynamic excitation: that is the case on EAC1 where the fundamental mode of the optical telescope assembly is about 10 Hz instead of about 1.5 Hz on LUVOIR-B.

**Interface Cable Stiffness Cancellation: EAC1 Evaluation**

Figure 5 illustrates the effectiveness of our cable stiffness pre-compensation logic when applied to Exploratory Analytical Case 1. That figure shows the principal gains of the transfer function matrix from the six DFP voice-coil actuator voltage commands as inputs to the six DFP relative position sensor readings as outputs prior to compensation (blue) and after compensation (red).

The collective stiffness of the harnesses referenced to the geometric center of the vibration isolation system interface is 50-bf/in in the linear degrees of freedom and 17.45 lbf-in/deg in the angular degrees-of-freedom as derived in the prior section, and the center of stiffness is at the geometric center of the isolation system interface by construction. Based on the EAC1 spacecraft and payload mass properties, the coupled system modal frequencies prior to cancellation are

[220;260;200;5.1;3.5;4.3]*milli-Hz. The associated mode shapes are dominantly Translation-X, Translation-Y, Translation-Z, Rotation-X, Rotation-Y, and Rotation-Z respectively in the relative pose degrees of freedom at the interface where Z is perpendicular to the interface plane. The relatively low natural frequency in the rotation degrees of freedom is due to the large payload and spacecraft central inertia. We set the modal damping ratio prior to compensation to 1%.

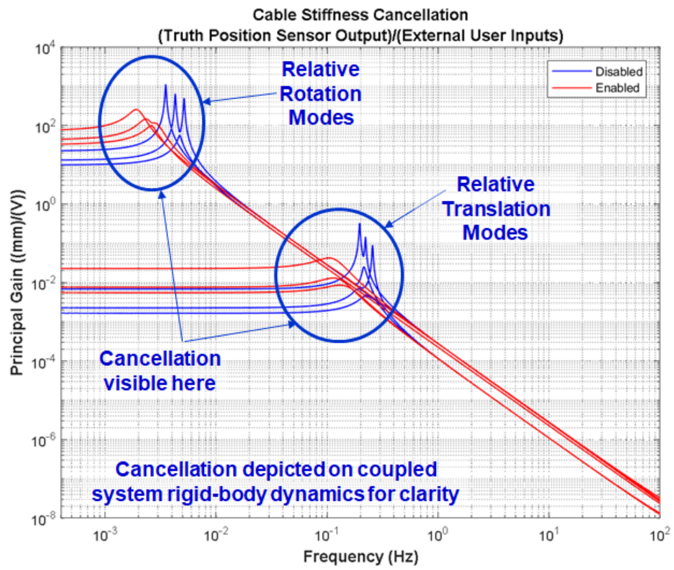


**Fig. 5** DFP control logic includes cable stiffness cancellation option and associated built-in test capability for on-orbit characterization.

We set the cable stiffness cancellation to 70% in the compensation logic. The results in Figure 5 show that the compensation logic reduces the modal frequencies by a factor of 1.8 as expected and reduces the amplification at resonance to a Q=3 or less. That cable stiffness cancellation pre-compensation allows us to close the relative position control loop in the DFP control system below the coupled system resonance: on EAC1 that relative position control logic operates at 0.11 Hz 0-dB cross-over bandwidth with a gain margin >11.6 dB and a phase margin >92.6 deg in the presence of the spacecraft flexible body dynamics.

### *3.2 Picometer Metrology*

The Habitable Worlds Observatory requires unprecedented stability to achieve the necessary 10 orders of magnitude contrast for direct imaging and characterization of Exo-Earths. That stability, on order of 2 pm over correlation times ranging from 10 msec to 1000 sec, will employ a wavefront control system (WFCS) to maintain wavefront errors of the observatory. A critical component of the WFCS is the external metrology system that measures the relative rigid body poses of the primary mirror segments, secondary mirror, and aft metering structure.

The baseline design for HWO includes a combination of long-distance laser metrology gauges (LDG) forming a laser metrology truss as well as edge sensors to perform this task. For this reason, the Ultra-Stable Observatory Roadmap Team (USORT) status report from July 2023 identifies small laser metrology sensors for primary to secondary measurements as a key technology gap.[19]

In this section, we provide technical updates on two laser metrology gauge technologies: 1) photonic-integrated-circuit-based (PIC) heterodyne laser gauges and 2) tracking frequency gauges. We also assess sensing configurations based on the initial configuration for Exploratory Analytical Case 1 (EAC-1). Finally, we assess installation tolerances for the PIC gauge technology only.

### *3.2.1 Photonic integrated circuit heterodyne laser gauge*

**Photonic Integrated Circuit heterodyne laser gauge overview.** For more than 20 years, Lockheed Martin (LM) has been maturing heterodyne laser metrology technology for use in space observatories. In the late 1990s and early 2000s, LM developed picometer-class free-space metrology gauges to monitor the distance and geometry of interferometer baseline collector telescopes for the Space Interferometry Mission (SIM).[20,21] LM further advanced this technology and patented a PIC-based integrated beam launcher capable of performing the same measurements in a more compact package.[22-24] LM continues to advance the design, by fabricating and testing new generations on both the TechMAST program and on internal funding.[25,26]

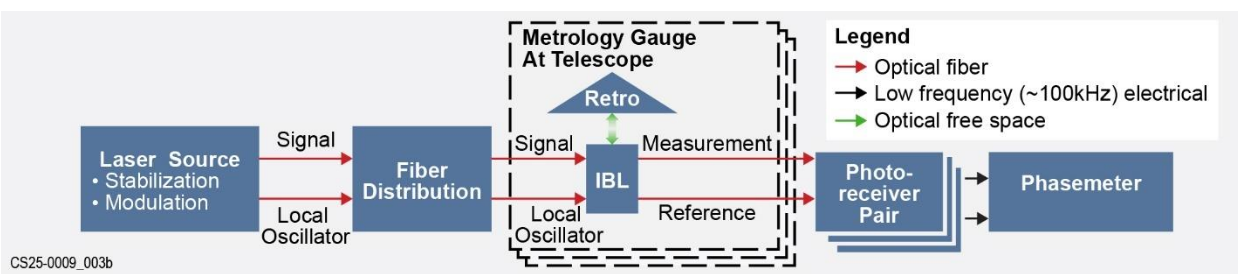


**Fig. 6** The components which comprise Lockheed Martin’s heterodyne laser metrology system**.**

Figure 6 shows the major components of LM’s heterodyne laser metrology system. A high-coherence, stabilized laser source is split and frequency shifted to form signal and local oscillator beams. These sources pass through a fiber distribution network to feed multiple metrology gauges at the telescope. The gauges consist of an integrated beam launcher (IBL) and a retroreflective fiducial. The IBL launches the signal beam to the retro, and the returned light is interferometrically combined with the local oscillator to form a measurable radio frequency (RF) beat frequency. A second reference interferometer internal to the gauge tracks common mode errors. The output of the metrology gauge feeds a photo-receiver pair and is post-processed via a phasemeter algorithm to generate the measurement and signal phases, which are subtracted to remove effects of propagation in the PIC itself. The measured phase is proportional to the linear displacement of the retroreflector relative to the IBL, providing a measurement of a single component of a mirror segment motion. Combining measurements from multiple metrology gauges for each segment allows for measuring the six degrees-of-freedom (DOF) position error of that segment, for real-time corrections by the active alignment system. This approach supports relative measurements between the primary to second structure of HWO by mounting the beam launchers to the primary segments and retro-reflectors to the secondary mirror.

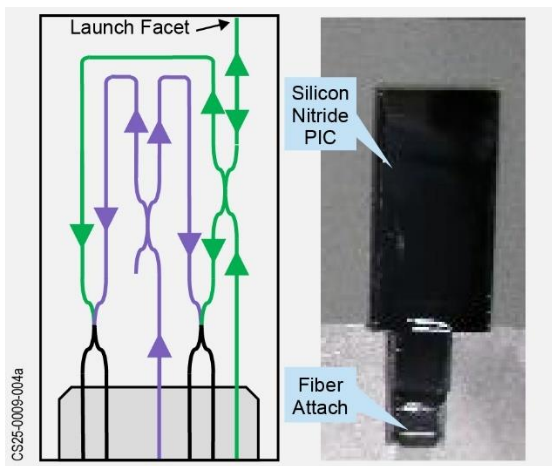


**Fig. 7** (Left) PIC waveguide layout. (Right) Silicon nitride PIC.

Figure 7 features a PIC, the primary component of the IBL, fabricated under TechMAST. The signal and local oscillators are input into the PIC and split to form two interferometer paths. The measurement interferometer directs one arm external to the PIC towards the retroreflector, which reflects light back into the PIC. The reference interferometer is maintained on PIC and measures common-mode error sources arising from disturbances (thermal, vibration) within the PIC itself. The difference in phase between the measurement and reference interferometers is proportional to the displacement between the PIC and retro-reflector.

Under the TechMAST effort, we devised and implemented a testbed to measure errors and drift internal to the PIC composed of largely commercial-off-the-shelf components. A high coherence 1550-nm laser (NKT Kohera Adjustik) feeds two fiber-coupled Gooch and Housego acousto-optic modulators (AOM). The modulators are driven by waveform generators at 40.0 MHz and 40.1 MHz to frequency shift transmitted light from the signal and local oscillator optical paths. These feed the input of the IBL. The beam launching output facet of the IBL is metallized to retro-reflect the signal and maintain all light on-chip. This method ensures a "zero-path" in which no displacement occurs, so any measured signal is inherent to the gauge itself, thus represents the noise floor of the gauge as accumulated from all sources in the signal chain. The IBL is placed within a vacuum chamber with thermal control consisting of passive water cooling and active PID heaters to minimize temperature variations. The signal and local oscillator path combine in the two interferometers resulting in a 100-kHz measurement and reference outputs. These outputs are fed to the photodetector (PD) pair, digitized, converted to phase, and then displacement via a phasemeter (PM) algorithm.

We performed metrology error measurements with the zero-path testbed over 8 hours to capture metrology errors from 0.001-100 Hz. Figure 8 shows the Allan Deviation –a measure of drift versus correlation time. The results show <12 pm of instability for correlation times <200 seconds.

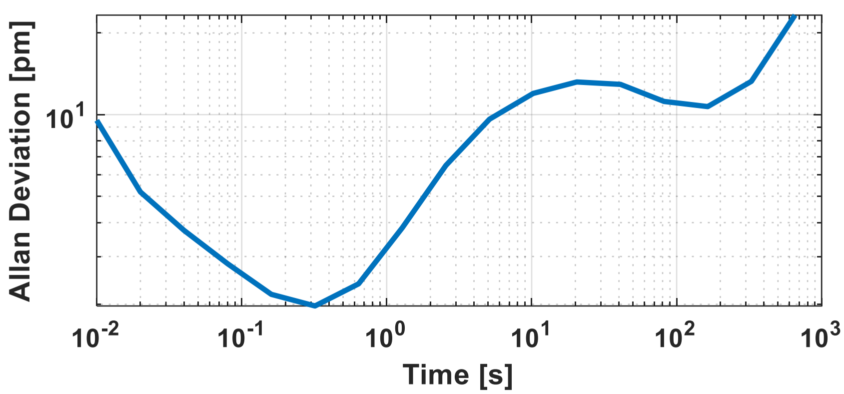


**Fig 8** Allan deviation of PIC internal measurement errors.

**Robustness to mechanical installation errors.** Another major challenge for the external metrology system is ensuring sufficient operational range to tolerate mechanical installation errors. This is especially true for the LDGs which must be accurately aligned from the primary mirror to be pointed at retroreflectors mounted up to 17 meters away on the secondary mirror. It is desirable for the metrology gauge components to be robust against these installation errors as to not require adjustment or realignment that could negatively impact the stability of the gauge measurement. We derive the required installation tolerances for a heterodyne laser metrology gauge by assessing radiometric losses. We assess these losses as a function of beam diameter for the beam launcher.

As a result, we recommend a beam diameter of 2 mm which maximizes pointing tolerances for the LDGs.

Optical losses on the gauge are dominated by free-space propagation from both spreading of the beam and mechanical installation errors, with a tradeoff between these two factors. As the beam expands, the peak irradiance at the return plane is reduced, but will span a larger area to reduce sensitivity to misalignment. The spreading is affected by the beam diameter of the launchers with smaller beams having greater divergence. To evaluate the trade, we assess the maximum tolerable losses from the free-space propagation of the metrology beam from either spread or installation errors. We then model losses for varying beam diameters and installation errors to determine the beam diameter that provides the best possible installation tolerances.

Acceptable losses are determined by calculating losses from all sources along the metrology gauges. This includes throughput of fiber optic distribution system, beam splitters, acousto-optic modulators, wavefront-error from the beam launcher, surface quality of the corner cube, and dihedral errors. We compare these losses, input optical power, and required return power to determine maximum acceptable losses of 53 dB for the combination of beam spreading and installation errors.

Installation errors can be simplified to a single beam offset parameter which is the perpendicular distance from the chief ray from the beam launcher to the vertex of the retro reflector. The return beam is translated by twice this offset value. Beam offset has significant sensitivity to the beam launcher orientation errors due to the large 17-m separation between the beam launcher and retro.

We model losses from installation errors via a numeric physical optics propagator. First, we define the initial beam profile of the gauge. We then perform Fresnel diffraction over 17 meters to the retro reflector. We add beam walk due to misalignment at the retro. We then perform Fresnel propagation back to the beam launcher. Then we calculate the fraction of the beam coupled into the gauge via the overlap integral

$$\left| \iint E_1^*(x,y)\, E_2(x,y) dx dy \right|^2$$

Where $E_1(x, y)$ is the propagated field of the beam and $E_2(x, y)$ is the normalized mode of the launch waveguide of the beam launcher at the pupil of the beam launcher, and * denotes complex conjugation. We found a beam-launcher with a 2-mm-beam provides 9.9 mm of allowable beam offset. We decompose this offset into a 100-um translational installation error and a 559-urad pointing installation error for the beam launcher.

In contrast to the LDGs, using laser gauges for edge sensing has much higher installation tolerances. Assuming a maximum separation of 10-cm between the beam launchers and the retro reflectors, heterodyne laser gauges can easily tolerate 8-mrad of orientation error. In addition, the gauges are agnostic to variation in separation between the beam launcher and retro-reflectors.

#### *3.2.2 Tracking frequency gauge*

The Tracking Frequency Laser Gauge (TFG) was conceived in 1990 at the Smithsonian Astrophysical Observatory as a candidate for the metrology component of POINTS,[27] a contender for the Space Interferometry Mission being developed there with NASA support. A US patent (5,412,474) on the TFG was issued to Reasenberg, Phillips, and Noecker in 1995 (and assigned to the Smithsonian Institution). The TFG was further described in Refs. 28-30.

The University of Florida (UF) and the Illinois Institute of Technology (IIT) are developing the TFG for picometer metrology for such missions as the proposed Habitable Worlds Observatory (HWO). This technology is useful both for segment-to-segment alignment and for primary-mirror to secondary-mirror alignment.

The TFG measurement principle relies on controlling and measuring laser frequency, rather than on measuring optical phase. As seen in Figure 9, a single reference laser, stabilized by an optical cavity or atomic line, is compared with N measurement lasers, each locked to a measurement interferometer (MI), whose length corresponds to the distance of interest, $L$. The TFG measures the change $\Delta f$ in the laser frequency corresponding to $\Delta L$. $L$ can range from centimeters to many meters with no loss of precision or accuracy.

Iter 2

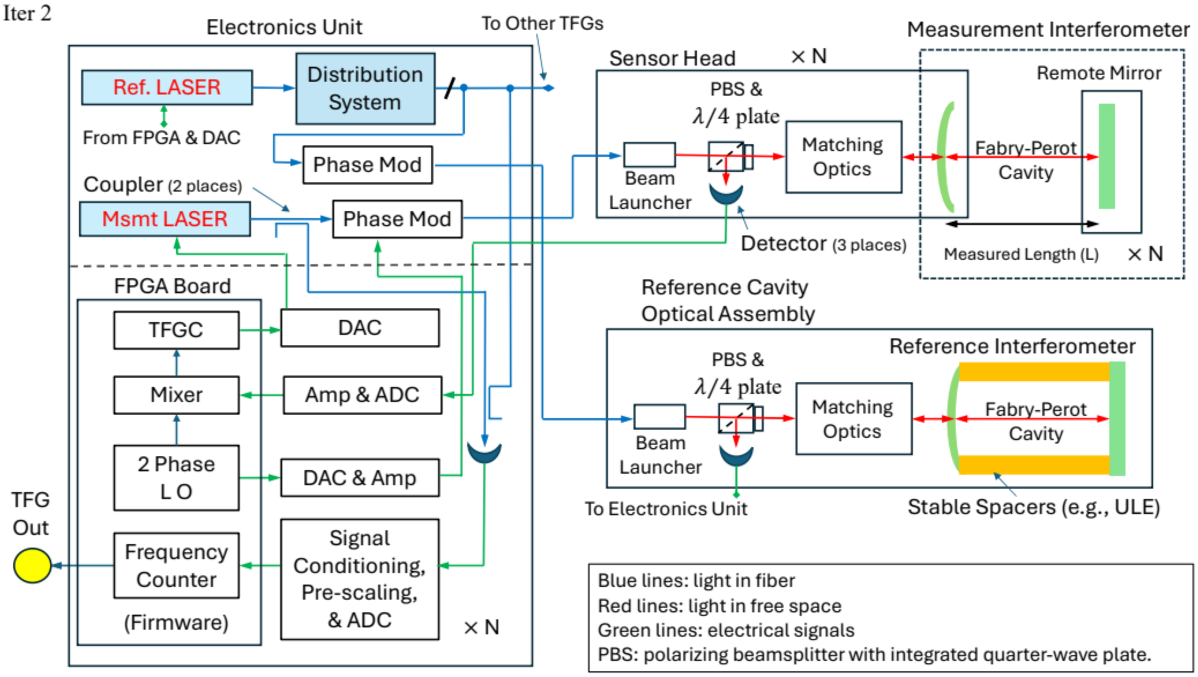


**Fig. 9** Opto-electronic design for TFG tests at IIT.

The TFG uses Pound–Drever–Hall (PDH) locking, in which a feedback controller (TFGC) continually adjusts the frequency of the measurement laser to be centered on the null of an MI. As $L$ varies in time (due e.g. to vibration or changes in temperature), the TFGC adjusts the laser frequency to track those changes. The resulting variation in frequency can easily be monitored by counting the beat between it and a sample from a stable reference laser. For each laser–MI combination, the change in beat frequency is proportional to the change in the distance measured. As $L$ varies, so does the frequency $f$ of the laser light:

$$\frac{\delta f}{\delta L} = \frac{2\Phi}{\lambda} = \frac{c}{\lambda\, L} \tag{1}$$

where $\Phi = \mathrm{c}/(2\mathrm{L})$ is the free spectral range, $\lambda = 1560$ nm (in our implementation) is the laser wavelength, and $c$ is the speed of light. Then, in general, $\delta f/\delta L = 1.92\,\mathrm{kHz/pm}\ (10\ \mathrm{cm}\ /\ L)\ (1560\ \mathrm{nm}/\lambda)$. The counting of cycles is a reliable operation if the frequency is not too high (Say, $f < 10\ GHz$, although the upper limit of counting electronics tends to rise over time and may well be higher when HWO is built). To translate the optical frequency to one that can be counted, a second TFG is locked to a high-stability cavity and samples of the two laser signals are combined on a detector, yielding the beat frequency.

If data are accumulated over a period $\tau$, then

$$\Delta N = 19.2 \text{ cycles } (\tau \ / \ 0.01 \text{ s}) \ (10 \text{ cm} \ / \ L) \ (1560 \text{ nm}/\lambda) \ (\Delta L/1 \text{ pm})). \qquad (2)$$

is the expected change in the cycle count during the period $\tau$ due to a length change ΔL. Discretization of the cycle count introduces a "perfectly correlated noise" with correlation coefficients of -1/2 between any datum and both the preceding and the following data.[31] At a sufficiently short count time $\tau$, this will dominate the white noise we normally see on the sub-second side of the TFG Allan deviation.

The TFG offers six advantages over other laser distance gauges: simplicity, measurement entirely in free-space with no glass in measurement path causing drift, wide range of operating distances, ability to measure absolute distance (cf. incremental distance normally measured), freedom from cyclic bias (typically the limiting factor for phase gauges), and ability to gain additional precision by operating in a resonant MI (finesse > 2).

Tests carried out more than a decade ago at the Center for Astrophysics |Harvard and Smithsonian (CfA) using a Fabry-Perot cavity (finesse = 130) as MI demonstrated incremental precision of 0.14 pm with $\tau = 1$ s, improving to 46 fm at $\tau = 50$ s.[28] Using a non-resonant (Michelson) interferometer at IIT, 0.9 pm at $\tau = 80$ s (incremental) and absolute accuracy of 0.17 μm at $\tau = 1000$ s have been achieved.[29] This absolute distance accuracy comes close to satisfying the criterion $\sigma(L) < \lambda/12 = 0.13$ μm for returning reliably to the same fringe after an interruption. While precision ideally improves linearly with finesse, only modest finesse is needed for HWO.

Preliminary results from the Ultra Stable Observatory Roadmap Team, a NASA-appointed committee chartered to provide technical analysis for HWO, require the measurements of the relative pose of HWO's adjacent mirror segments to have an uncertainty of 1 to 3 pm over time scales from under 10-ms to hours or days. Figure 10 shows the result of a laboratory experiment conducted by differencing the outputs from two TFGs on a common-path test-bed in air: the measurement instability achieved is <3 pm over correlation times ranging anywhere from 3 msec to 2.8 hours in that configuration.

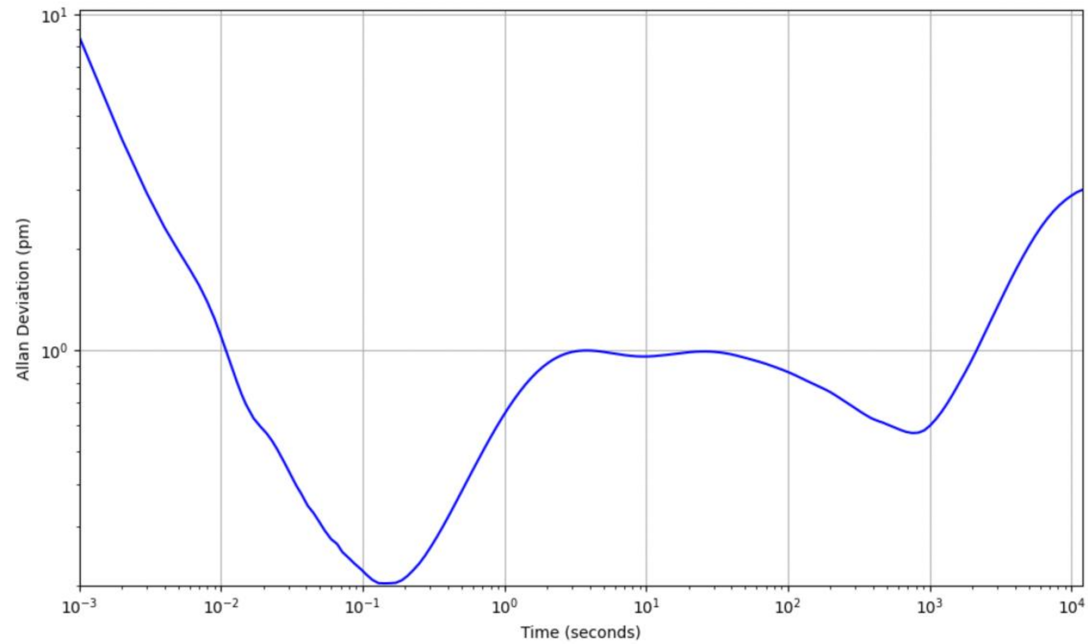


**Fig. 10** Allan deviation vs. averaging time of a recent TFG test run in optical cavity at IIT.

The Allan deviation shown in Figure 10 was obtained using the CfA optical cavity (finesse = 130) and a TFGC implemented in an FPGA (Red Pitaya). That cavity has a larger free spectral range (FSR) than the Michelson interferometer previously used. Two TFGs were locked to adjacent nulls of the cavity, which was in air, so that their beat signal was nominally the FSR of about 600 MHz. This is beyond the capacity of our current frequency counter. As a short-term fix, we inserted an available divide-by-nine circuit ahead of the counter in addition to its internal (fixed) divide-by-two circuit. This resulted in an increase in the perfectly correlated noise, which shows up in the Allan deviation as a slope of -1 for periods under 0.1 s. For comparison, note that white noise would manifest a slope of -1/2 in the Allan deviation plot.

Current efforts are underway at both UF and IIT to improve the performance of the current TFG layout. UF is working on the development of a simulation of the setup for better error modeling of the system. This effort focuses on a time-domain Simulink simulation following the architecture currently in place at IIT. By modeling the interferometer response along with the currently implemented PID feedback, a better understanding of the coupling of noise into and stability of the system can be achieved.

At IIT progress is being made on the feedback control of the PDH lock and corresponding loop frequency response. The acquisition of a faster counter is being investigated. The current Allan deviation, which is scaled by $\sqrt{2}$ under the assumption that the two TFGs have comparable Allan deviations, is below a picometer from 10 ms up to at least 1000 s, reaching a minimum of 200 fm. We continue to investigate limiting noise sources .

The team at UF and IIT, in collaboration with Lockheed Martin, are continuing to progress towards a complete TFG error model and noise mitigation of the experimental setup. We are investigating novel solutions to increase the allowable mechanical installation tolerance, along with estimating the current installation-tolerance requirements. We are working on refining the beam launcher design to minimize the number of optical elements, while maintaining the required optical mode matching. Future work is planned to include the introduction of a stable reference cavity placed along with the current MI under vacuum. This will more closely align the experimental setup to the final configuration that has been proposed for use in spaceflight.

#### *3.2.3 Optical Edge Sensing and Long-Distance Metrology Configuration and Mechanical Integration*

A primary challenge for HWO is the placement, orientation, and count of metrology gauges, which impacts the control systems performance to stabilize the wavefront. In addition to minimizing wavefront error, the metrology configuration should minimize concessions on coronagraph contrast by limiting gap size between primary mirror segments and consider complexity on installation of metrology gauges. We assess alternative metrology configurations for HWO's EAC-1 not previously considered. We present an alternative edge sensing configuration that improves the control system's performance and relaxes requirements for count and locations of long-distance laser gauges –allowing for the elimination of these gauges between primary mirror segments. Given this configuration, we assess requirements on installation tolerances of a heterodyne laser metrology gauge.

Figure 11 illustrates the optical telescope assembly for EAC-1 which consists of 19 primary mirror segments, and an off axis secondary mirror. Also included is the aft metering structure which is treated as rigid structure for this assessment. EAC-1 has 6 LDGs on each primary mirror segment, and an additional 6 LDGs on the aft metering structure. These LDGs are paired with one of 12 retroreflectors mounted on the secondary mirror forming the laser metrology truss. EAC-1 also contains 2 capacitive edge sensors at each adjoining edge between primary mirror segments with each sensor providing 3 orthogonal measurements for piston, gap, and shear. In total, EAC-1 considers 120 candidate LDG measurements and 252 edge sensing measurements. These measurements provide feedback to rigid body actuators to stabilize the relative pose of the OTA components as a portion of the overall wavefront control system.

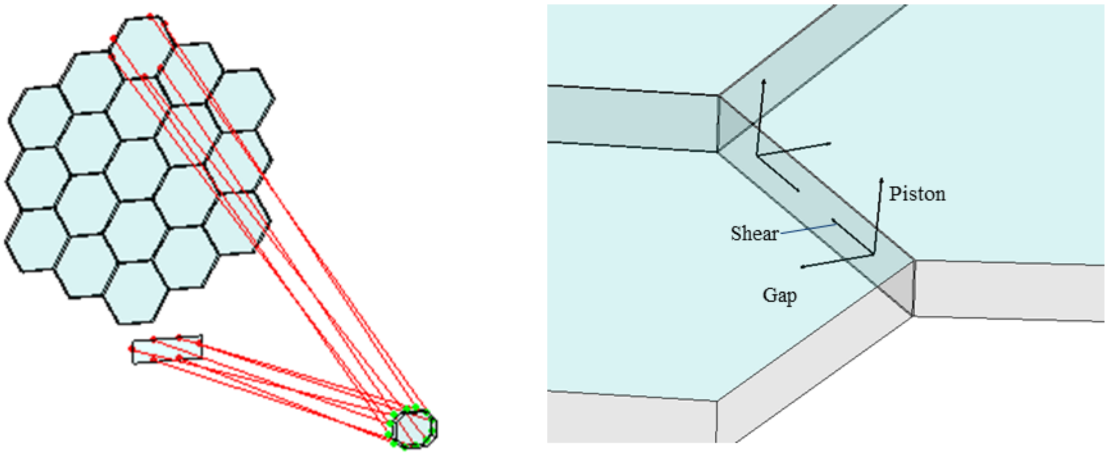


**Fig. 11** Left: Optical Telescope Assembly with a sample laser metrology truss for one primary segment and the aft metering structure. Right: Edge sensor location and measurement directions for EAC-1 sensors.

A linear optical model (LOM) of EAC-1 was provided by the HWO project office. The LOM contains a linear sensitivity analysis with resulting wavefront error given 6 degree-of-freedom rigid body perturbations. We assume the aft metering structure is a rigid structure.

To score the metrology configurations we use the wavefront error multiplier (WEM) originally proposed by the Jet Propulsion Laboratory (JPL)[32] and is the ratio between closed-loop wavefront stability and metrology gauge error. In JPL's assessment, they calculate WEM for configurations in which combinations of edge sensor piston, shear, gap, and LDG measurements are removed. They deem a configuration successful if the WEM has a value of 2 or less. As the LOM has undergone iteration since the publishing of JPL's results, we show resulting WEM for the cases in which all metrology measurements have equivalent errors in Figure 12. Each column of the figure represents the number of primary segments that maintain their LDGs as well as the aft metering structure while the rows represent which sensing axes of the edge sensors are active. While there are some minor differences with the original JPL results, trends remain the same.

| PM + SM Laser Trusses | 20 | 14 | 11 | 10 | 8 | 6 | 5 | 4 | 2 | 1+Perim |
|---|---|---|---|---|---|---|---|---|---|---|
| Piston, Gap, & Shear | 0.78 | 1.09 | 1.18 | 1.23 | 1.30 | 1.90 | 2.54 | 2.79 | 8.34 | 2.56 |
| Piston and Gap | 0.79 | 1.10 | 1.19 | 1.24 | 1.32 | 1.93 | 2.61 | 2.86 | 9.20 | 2.66 |
| Piston and Shear | 0.92 | 2.08 | 4.57 | 5.53 | 5.32 | 298 | 895 | 1060 | 26700 | 3.02 |
| Piston Only | 1.34 | 2130 | 2300 | 2460 | 2650 | 10200 | Inf | Inf | Inf | 9.32 |
| Gap Only | 1.48 | 95500 | 68200 | 74900 | 58700 | 98300 | Inf | Inf | Inf | 180000 |
| Shear Only | 3.74 | 72500 | 153000 | 140000 | 142000 | 198000 | Inf | Inf | Inf | 122000 |
| Gap and Shear | 1.17 | 25.1 | 29.1 | 29.5 | 32.3 | 35.0 | 46.3 | 48.7 | 72.6 | 85.1 |
| No Edge Sensors | 10.9 | Inf | Inf | Inf | Inf | Inf | Inf | Inf | Inf | Inf |

WEM < 2.0
WEM > 10.9

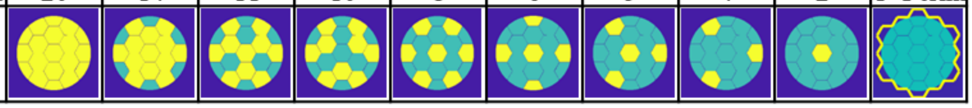

**Fig. 12** Wavefront error multiplier (WEM) for various external metrology configurations including an alternative configuration with LDGs only at the outside perimeter of the primary mirror. Green cases represent a WEM <2 and red a WEM>10.9.

We consider an additional configuration the previous analysis did not: using only LDGs on the perimeter of the primary mirror. This configuration would not require any LDG between primary mirror segments allowing gaps between segments minimized. This configuration with all edges sensing measurements results in an almost-acceptable WEM of 2.56 (top right configuration of Figure 12).

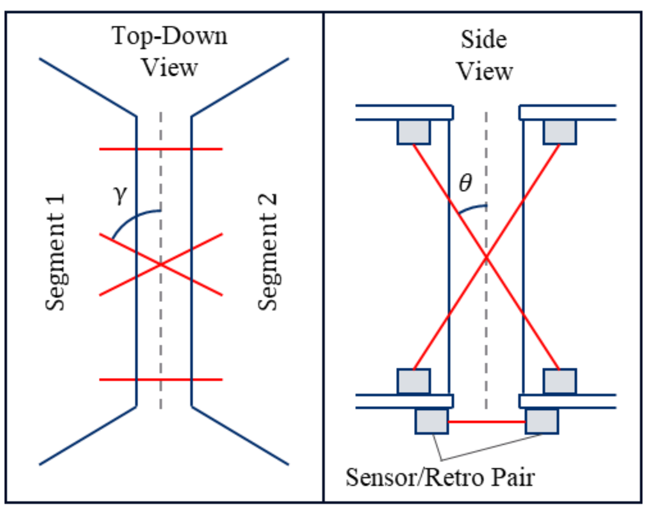


**Fig. 13** Alternative edge sensing configuration using 6 pairs of crossed laser metrology gauges.

An alternative approach to edge sensor architecture was then developed to attempt to reduce the WEM by more strongly sensing what are otherwise only weakly sensed degrees of freedom in the traditional edge sensor architecture. Figure 13 illustrates a method of edge sensing using 6 laser metrology gauges: 2 pairs of crossed gauges oriented at an angle $\theta$, and 1 crossed pair mounted on the back face of the mirrors with an angle $\gamma$. Figure 14 shows WEM as a function of $\theta$ and $\gamma$ for two configurations: 1) with all LDG and 2) for removing all LDGs internal the primary mirror. The results highlight importance of the piston degree of freedom with greater WEM at lower $\theta$, and low sensitivity to $\gamma$. Optimal configurations occur for both cases when $\theta = 10°$ and $\gamma = 50°$, assuming a minimum attainable angle of 10°. The alternate edge sensing configurations provide an 18% improvement in WEM for the all-LDG case and a 29% improvement for the perimeter only LDG case with the end WEM of 1.73 –achieving the desired <2.0 WEM value.

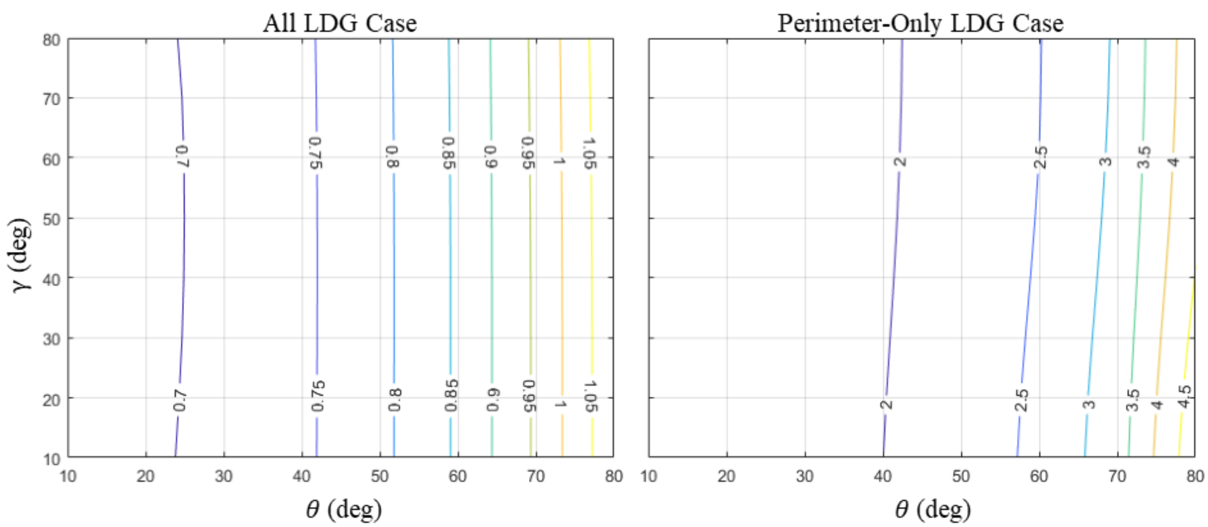


**Fig. 14** WEM using alternative edge sensing configuration as a function of $\theta$, and $\gamma$. Left: using all LDG, Right: using perimeter only LDG.

Using a combination of laser metrology gauges for edge sensing and perimeter-only gauges for the laser metrology truss provides an acceptable WEM. More importantly, this configuration eliminates requirements for larger gaps between primary mirror segments to support both larger laser beam diameters and line of sight to the retro reflectors on the secondary mirror. The presented edge sensing configuration is made possible using laser metrology gauges.

There are more opportunities to further reduce WEM not considered. We limit potential locations of long-distance gauges to 120 candidate locations from EAC-1. More gauges can be added and their positions and can be tuned to optimize WEM. Future work should also consider redundancy of measurements to reduce risk from gauge failures.

### *3.3 Optical Telescope Assembly Structural Damping Augmentation*

All telescopes are susceptible to degradations in performance due to structural deformations of the supporting structure. For static deformations (gravity sag, *etc*.), these degradations are addressed with enhanced structural stiffness and low frequency-bandwidth optical compensating actuators. For frequencies above the capability of these low-bandwidth actuators, the dynamics of the structure dominate, such as disturbances from attitude positioning actuator noise, cryocoolers, thermal snap, ring down from pointing slews, *etc*. resulting in structural vibrations that degrade the optical performance. Certainly, stiffness enhancement will help reduce these effects by pushing modal frequencies higher and potentially above range of concern and reducing response levels for modes that do remain in the bandwidth of concern. But, as accuracy and precision requirements increase, it becomes increasingly difficult to just stiffen one's way out of the problem. Enhancing the structural dynamics by intentional augmentation of damping into the system is one tool that can be used to mitigate these dynamic effects and meet performance requirements. The extreme optical performance requirements of Habitable Worlds Observatory (HWO) may necessitate damping augmentation into the system. Moog has developed a powerful array of damping and vibration mitigation technologies over the past 40+ years, ranging from pure damping to isolation, passive and active technologies. All have been realized in practical solutions, and many have space flight heritage. The finite element model of the EAC1 (Exploratory Analytical Case 1) configuration has been used to propose and evaluate candidate damping measures. We have primarily focused on the payload (optical) side of observatory under the assumption that the isolation system between the spacecraft and payload is highly effective. Furthermore, at least initially, the focus has been on the dynamics of the modes encompassing the lower bending modes of the observatory and the first few suspension modes of the mirror segment support/positioning system. We have focused our attention on a few areas of the structure where we can be reasonably certain that they will significantly impact the optical performance: overall supporting truss structure of observatory; secondary mirror support structure; and primary mirror support actuators.

Several technologies were examined for the secondary mirror support structure: co-cured viscoelastics,[33,34] passive tuned mass dampers,[35,36] and active tuned mass dampers.[37,38] With much of the truss structure for the telescope being nominally constructed with composite materials, this offers an opportunity for applying viscoelastic materials. Traditionally, viscoelastics have been eschewed for optical systems due to concern about outgassing from the viscoelastic material contaminating the optical surfaces. With a co-curing layup, however, the viscoelastic material is encapsulated inside the composite layup largely alleviating these concerns. Co-cured viscoelastic damping can achieve significant damping levels across a broad range of frequencies. Using the Modal Strain Energy approach, it was estimated that between 0.5% critical to almost 3.5% critical damping could be added across a broad range of modal frequencies. With passive tuned mass dampers (TMDs), a mass-spring-dashpot system is added to the structure in an advantageous location to target a specific structural mode with the size of the TMD set according to the modal dynamic properties of the host structure. Typically, one TMD is required to damp each targeted mode. In this study, TMDs were evaluated assuming that they would be mounted in a location behind the secondary mirror, *i.e.* at the end of the long cantilever truss support structure. It was found that to achieve 5% critical damping in all of the significant secondary mirror bending modes up to 50 Hz, a total of 10 TMDs would be required with a total added mass of more than 1500 kg. On the other hand, an active TMD can target multiple modes simultaneously and is sized based on disturbance levels in the host. For this study, a pair of active TMDs located behind the secondary mirror could damp the same 10 secondary mirror truss bending modes with damping levels ranging from 1.4% to 7.8% of critical with an added mass of only 70 kg. The active TMDs are clearly the much better option for targeting these modes and have been recommended for further pursuit. Figure 15 shows the open and closed-loop responses for one axis of the active TMD illustrating the broadband and high damping levels that are achievable. It should be noted that the 5 Hz resonance in Figure 15 is the internal resonance of the active TMD while the higher resonances are the bending modes of the secondary mirror tower of the observatory.

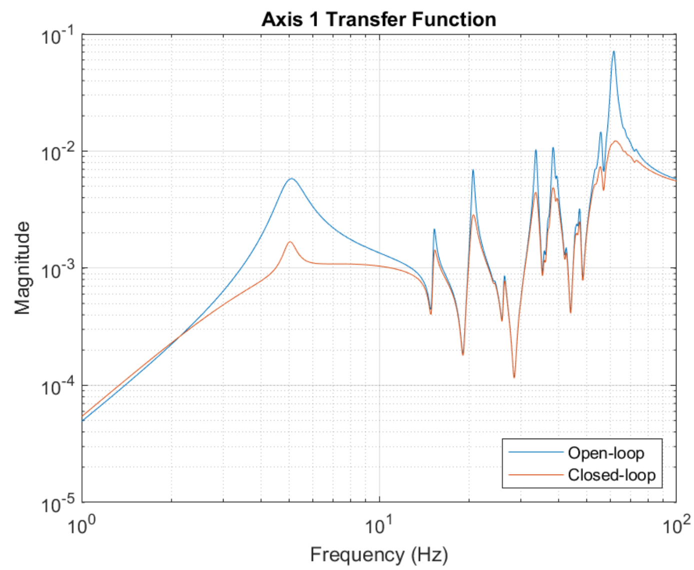


**Fig. 15** Open and closed-loop response plots showing benefit of active tuned mass damping for secondary mirror support structure.

In the second part of the study, attention was turned to the mirror support-positioning system, which consists of a hexapod mount and two-stage positioning system. The two-stage system is somewhat notional at this point but was assumed to be a coarse positioning stage and a fine (picometer) positioning stage. For the picometer stage, it was assumed that the actuation would be performed with either piezoelectric or electro-strictive actuators capable of the high force, but low strain required for picometer positioning. The frequency bandwidth of these actuators is way beyond that needed for the positioning application and extends well past the suspension modes of the mirror. Since all the corrupting energy from the telescope structure must pass through these actuators to reach the mirror segments, this offers the potential for utilizing the extra actuator capability to add damping to these optically significant mirror suspension modes. In the study, active damping control was evaluated using the piezoelectric actuators and a collocated strain sensor.[39,40] As shown in Figure 16, significant damping was added to all the mirror suspension modes up to 100 Hz, with closed-loop damping levels between 4.2% to 9.5% critical for the six suspension modes. It was also demonstrated that the required piezoelectric actuator forces during slewing and steady-state operations is well within the capabilities of these actuators.

During this damping augmentation study, it was shown that there are several viable damping augmentation technologies that can be readily brought to bear on the HWO. Further, it was shown that all of the optically significant modes of the telescope assembly could be augmented with damping levels ranging from at least 1.4% to as much as 9.5% critical. Early examination of these damping technologies ensures that they can be more easily designed into the system up front rather than the after-the-fact *ad hoc* approach typically employed.

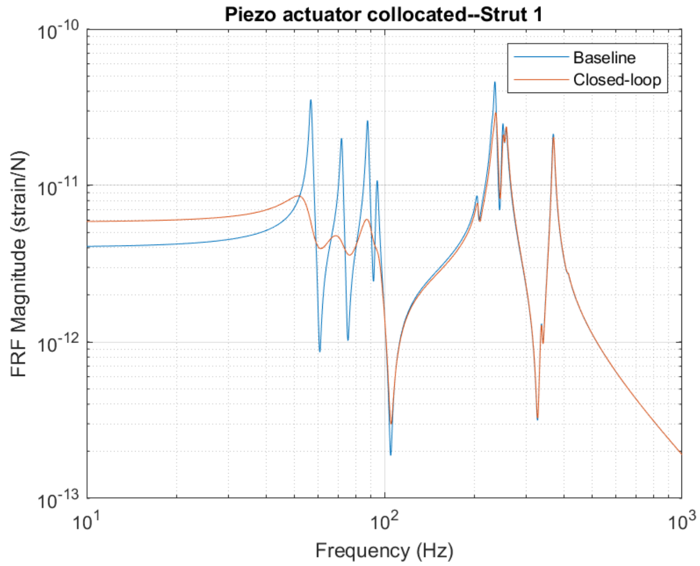


**Fig. 16** Open and closed-loop response plots showing benefit of active damping control for picometer positioning system.

### *3.4 Cryogenic Detector Cooling For Mission Yield Enhancements*

The primary mission of the Habitable Worlds Observatory (HWO) is to directly image 25 potentially earth-like planets orbiting nearby stars using coronagraphy, and to measure the spectra of the atmospheres of those planets, looking for signatures of possible life such as $O_2$, $O_3$, and $CH_4$ in the presence of $O_2$ or $O_3$.

The publication by Howe, Stark and Sadleir[4] details the predicted benefit of an energy resolving detector (ERD) which allows multiple planetary spectra to be measured simultaneously while observing a star's planets. The paper concludes that the number of spectra measured for earth-like planets will be approximately 30% higher with ERDs than without. This predicted benefit may become the difference between meeting the primary science criterion or failing to meet it. Candidate ERDs are Transition Edge Sensors (TES)[41] and Magnetic Kinetic Induction Detectors (MKID),[42] which operate below 1 K and thus require active cooling, so if they are to be considered for HWO, a means to provide the cooling without introducing unacceptable vibration during observations is required. On this effort, we identified several cryocooler configurations and formally scored them following the Kepner Tregoe Analysis (KTA) of alternatives process to arrive at a preferred cooling configuration.

Cooling below 1 K requires two stages of cooling, typically an adiabatic demagnetization refrigerator (ADR) or dilution refrigerator (DR) precooled by liquid helium and/or a mechanical cryocooler such as a Stirling, Brayton, or Joule Thomson (JT) cryocooler. While an ADR should have no perceptible vibration, mechanical cryocoolers are a source of vibration, ranging from tens or hundreds of mN for Stirling or JT cryocoolers such as that used on the Mid-Infrared Instrument (MIRI), or several mN for Brayton or sorption-type JT cryocoolers.

We selected the continuous ADR (CADR) as the detector cooler, due to the maturity of the CADR developed by NASA's Goddard Space Flight Center. While the Planck space telescope used a DR to cool a detector to 100 mK, we see no compelling reason to pursue the DR option at present. There are two CADR options, rejecting heat either at around 4 K or at around 10 K. The latter CADR is still under development but has been demonstrated in the laboratory.[43]

The options for the precooler included a solid hydrogen cryostat, basing parameters such as mass and lifetime on the WISE[44] and Spirit III[45] solid hydrogen dewars, and Brayton cryocoolers, which offer relatively low exported vibration. For Brayton cryocoolers, we included a 3-stage Brayton providing cooling at 10 K[46] and a 4-stage Brayton or Brayton/JT hybrid providing cooling at 4 K.[47]

We also included an option to duty-cycle the precooler by using it to cool a thermal storage device, a block of solid hydrogen in the case of a CADR rejecting heat at 10 K, or a block of gadolinium oxysulfide (GOS) rare earth material with high heat capacity at 4 K for the CADR rejecting heat at 4 K. For duty-cycled cooling, the CADR runs continuously, while the precooler is turned off during observations. We assumed that the precooler is on for 5% of the time and off for 95%, and that a maximum observation period of 5 days would be required, based on parameters in signature science case #1 of the LUVOIR Final Report.[15] This duty cycle and observation time affect the mass and volume of the thermal storage device (if any), and the mass of a solid hydrogen precooler as well as the mass and electrical power of a Brayton precooler.

We based our trade of alternatives on two "must have" capabilities and 12 desired features used for scoring the various options. Table 3 summarizes our scoring results. The scores in that KTA table should be interpreted strictly as representing relative rankings from low to high. An option receiving the highest score against "ease of packaging" for instance means we assess that option as being easier to package than the others; it does necessarily mean that option is easy to package.

The configuration with the highest score is the 4 K Brayton cryocooler with a 5% duty cycle, cooling a rare earth thermal storage device into which a 4 K CADR rejects its heat continuously. Figure 17 summarizes its main characteristics. We selected that cryocooler configuration for packaging feasibility studies on the coronagraph instrument as the next step. That packaging needs to consider electrical power dissipation and power dissipation fluctuations. As shown in Figure 17, while preferred, we anticipate that option will be challenging to package within a serviceable coronagraph instrument due to the amount of power dissipation (375 W) and its envelope dimensions (26 in x 11 in x 20 in).

The recommended cryocooler configuration requires some technology maturation to bring the system to TRL 5. First, the 4 K Brayton precooler requires complete cryocooler development and testing. A 10 K Brayton has been tested,[46] and a 4 K turboalternator has been tested,[47] but a complete 4 K Brayton cryocooler has not yet been built and tested. Second, the rare earth thermal storage device needs to be designed and tested. The rare earth GOS material must be packaged with a thermally conductive material such as aluminum, must be designed to survive launch vibration and thermal cycles between ambient and 4 K, and must include thermal interfaces to both the CADR and the Brayton. Finally, the cryogenic detector itself requires maturation, with TES requiring more pixels than have been previously implemented, and MKIDs requiring higher energy resolution.

**Table 3** Kepner Tregoe Analysis of cryocooler configuration options.

| | **Score** | **Weight** | **Solid H2 + 10K CADR** | **Continuous 4K Brayton + CADR** | **5% Duty Cycle 4K Brayton + CADR** | **Continuous 10K Brayton + CADR** | **5% Duty Cycle 10K Brayton + CADR** |
|---|---|---|---|---|---|---|---|
| **Must Have** | | | | | | | |
| Instrument Readily Serviceable (Cryocooler housed entirely within instrument) | | | **1** | **1** | **1** | **1** | **1** |
| Capability to cool to 50 mK | | | 1 | 1 | 1 | 1 | 1 |
| **Want** | | | | | | | |
| Low Volume | 0-10 | 2 | 1 | 7 | 7 | 7 | 0 |
| Low Mass | 0-10 | 3 | 0 | 9 | 4 | 8 | 2 |
| High TRL | 0-10 | 6 | 5 | 10 | 9 | 9 | 4 |
| Flight Heritage | 1-10 | 4 | 7 | 7 | 4 | 4 | 4 |
| No Solid Cryogens Required | 0-10 | 6 | 0 | 10 | 10 | 10 | 0 |
| Long Instrument Lifetime Between Servicing | 0-10 | 5 | 1 | 10 | 10 | 10 | 10 |
| No Vibration During Observations | 0-10 | 10 | 10 | 0 | 10 | 0 | 10 |

| | | | | | | | |
|---|---|---|---|---|---|---|---|
| Instrument Warm When Launched | 0-10 | 4 | 0 | 10 | 10 | 10 | 0 |
| Low Electrical Input Power | 0-10 | 5 | 10 | 3 | 7 | 4 | 4 |
| Small Thermal Swings from Power Cycling | 0-10 | 4 | 10 | 10 | 0 | 10 | 0 |
| Short Time Added Between Observations | 0-10 | 1 | 10 | 10 | 0 | 10 | 0 |
| Ease of Packaging into instrument | 0-10 | 5 | 1 | 7 | 7 | 7 | 0 |
| **Total Score** | | | 270 | 379 | **416** | 363 | 216 |

**Table 4** Kepner Tregoe Analysis Scoring rationale.

| | |
|---|---|
| Low Volume | Linear scale, maximum volume among options = 0, zero volume = 10 |
| Low Mass | Linear scale, maximum mass among options = 0, zero mass = 10 |
| High TRL | Solid hydrogen, 4K Brayton, and 10 K CADR all require higher TRL |
| Flight Heritage | -3 points for each subsystem that has not flown (CADR, Precooler, Thermal Storage Device) |
| No Solid Cryogens Required | Solid cryogens can be troublesome: additional vacuum GSE and on-launchpad servicing required |
| Long Instrument Lifetime Between Servicing | Score = Number of years of instrument lifetime |
| No Vibration During Observations | Continuous Brayton is a source of mN vibrations |
| Warm Instrument When Launched | If instrument must launch at cryo temperature, it complicates CONOPS and outgassing |
| Low Electrical Input Power | Based on power estimates from Creare LLC [47] |
| Small Thermal Swings from Power Cycling | Powering the cryocooler on and off introduces temperature swings at cryocooler's radiator. This could be mitigated with trim heaters. |
| Short Time Added Between Observations | Recharging thermal storage device adds downtime equal to 5% of observation time |
| Ease of Packaging into instrument | Currently uses the same scoring as "Low Volume" |

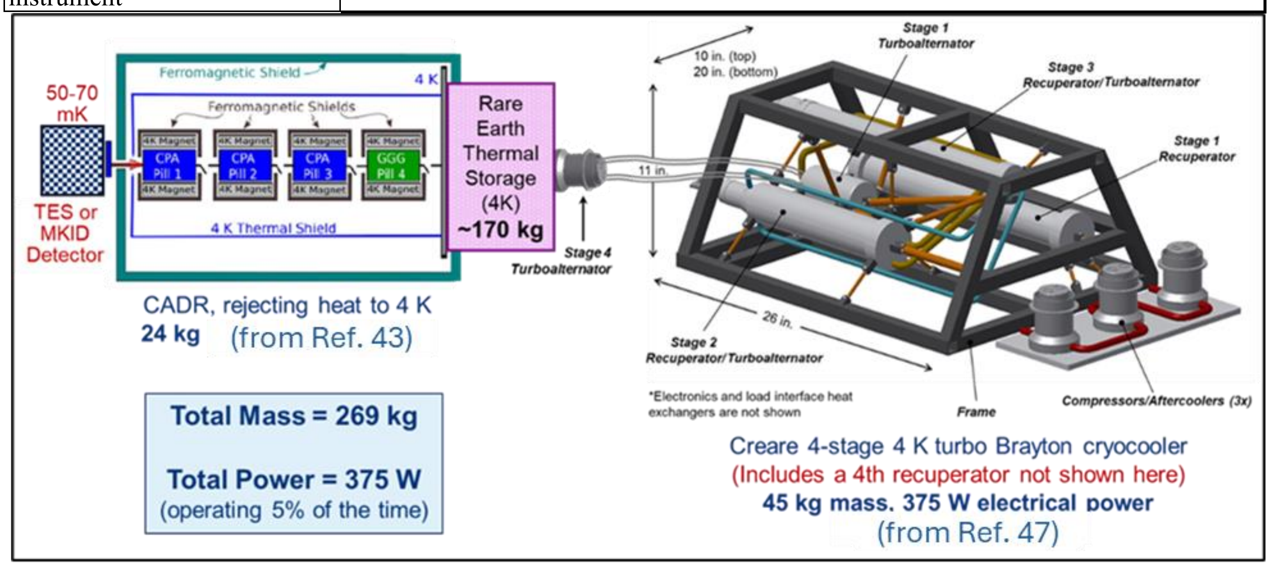


**Fig. 17** Description of Preferred Crygenic Detector Cooling System Configuration Selected For Packaging Studies.

## 4 Evaluation of Exploratory Analytical Case 1 Pathfinder Architecture

In this section, we evaluate the performance of the Disturbance Free Payload system, and the line-of-sight stabilization system as applied to NASA Exploratory Analytical Case 1. That evaluation includes rejection of spacecraft vibrations originating from the reaction-wheels, dynamics line-of-sight stability, and dynamic wavefront stability.

### *4.1 Structures, Optics, and Controls Integrated Model*

For this work, the NASA Integrated Modeling team provided NASTRAN structural dynamics models of the observatory in the deployed configuration. We decomposed that model into separate structural dynamics models, one for the spacecraft and one for the payload as depicted in Figure 18. We extracted normal modes up to 200 Hz and performed model reduction on both to achieve manageable model complexity while retaining the dominant dynamics characteristics. For the payload, we applied balanced model order reduction using dynamic wavefront error as the scoring metric and retained the 220 most significant structural modes ensuring that 98% of wavefront error is captured (threshold below 0.3 pm/uN). For the spacecraft, we applied balanced model order reduction using spacecraft inertial pose at the mechanical interface between the spacecraft and the payload as the metric: we retained the 194 most significant structural modes ensuring that more than 99.98% of the pose errors is captured. The fundamental mode of the spacecraft is 0.048 Hz and the fundamental mode of the payload is 10.67 Hz (secondary mirror tower bending mode).

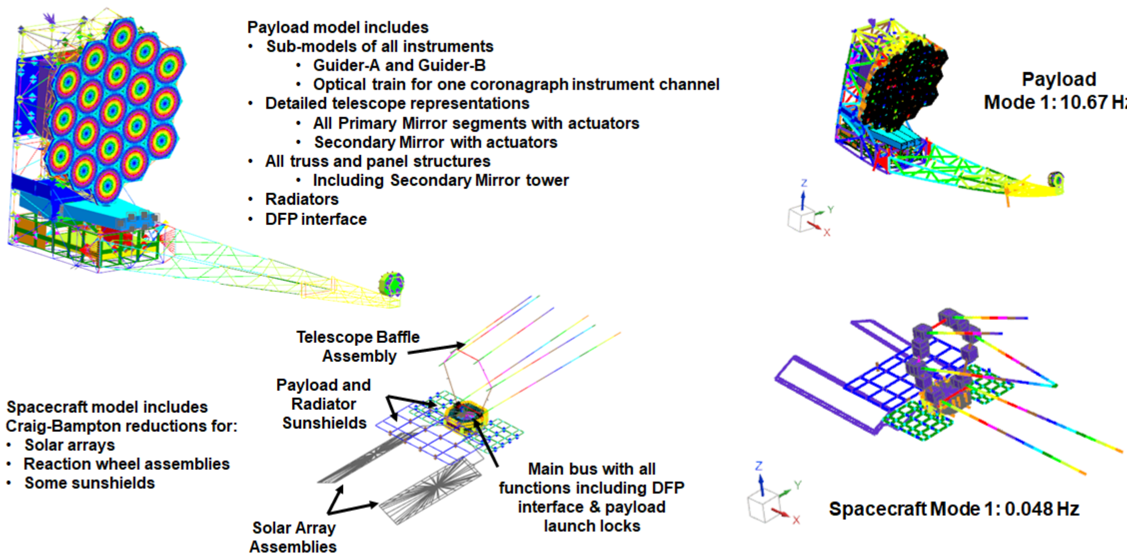


**Fig. 18** Overview of Payload and Spacecraft Structural Dynamics Models.

For this work, the NASA Integrated Modeling team also provided a linear optical model and the optical sensitivities for the line-of-sight and the optical path difference for one of the coronagraph instrument visible channels up to the focal plane mask. We coupled those optical sensitivities with the payload structural model and replaced one of the fixed mirrors in that coronagraph optical train by a heritage passive reaction-cancelling Fast-Steering Mirror for line-of-sight stabilization (that fixed mirror was already designated to become a steering mirror). We model the Fast-Steering Mirror exported forces and torques. Finally, the NASA Integrated Modeling team also provided the line-of-sight optical sensitivities for two guider instruments, which we interfaced to the structural dynamics model for payload attitude determination.

Our dynamics modeling and simulation environment includes large-angle flexible-body capabilities to simulate large angle slews. Since they do not capture non-linear kinematics, Finite-Element structural models are not suitable for large-angle flexible-body dynamics and therefore not suited for slew simulations in their native form. Our dynamics models combine large-angle rigid-body dynamics and small-deflection flexible-body dynamics to support slew simulations and settling analyses past the end of the slew. The Finite Element analysis provides the inputs necessary to construct the flexible-body dynamics portion of those models. That environment facilitates switching between pure rigid-body dynamics for control logic synthesis and troubleshooting, and flexible-body dynamics for high-fidelity time simulations.

Our integrated models include high-fidelity representation of the DFP actuators, relative position sensors, and control logic. A Payload Attitude Determination System (ADS) using a multiplicative extended Kalman filter fuses the outputs from the 3 Star Trackers, the 2 Fine Guidance Sensors, and an Inertial Reference Unit. DFP uses the ADS estimated payload inertial attitude and inertial angular velocity for payload inertial attitude control. Changes in alignment of the ADS sensors relative to the Payload reference frame datum due to structural deformations under dynamic conditions are captured.

Our integrated modeling and simulation environment supports both frequency-domain analysis for control synthesis and control system stability margin assessment, and time-domain analysis for dynamic line-of-sight and dynamic wavefront error performance assessment.

### *4.2 Design Departure Point Overview*

**Table 5** Design Departure Point Configuration.

| Habitable World Observatory: Spacecraft/Payload Non-Contact Design Baseline | | | | | |
|---|---|---|---|---|---|
| # | Group | Subgroup | Select Parameters | Value | Comments/Assmptions |
| 1 | DFP | | Actuator Mounting Radius | 145.56 cm | • |
| 2 | DFP | Non-Contract Voice-Coil Actuators | Stroke | +/-10 mm | • Increases at lower relative pose control bandwidth for given slew agility |
| 3 | DFP | Non-Contract Voice-Coil Actuators | Gap | 12 mm | • Gap between coil assembly and field assembly at mid-stroke |
| 4 | DFP | Non-Contract Voice-Coil Actuators | Force Constant | 5.0-5.5 N/Amp | • Varies over range; same as Back-EMF constant in SI units |
| 5 | DFP | Non-Contract Voice-Coil Actuators | Peak Force | 10 N | • Driven by slew agility and cable preset |
| 6 | DFP | Non-Contract Voice-Coil Actuators | Continuous Force | 5 N | • Driven by cable preset |
| 7 | DFP | Non-Contract Voice-Coil Actuators | Current Drive Peak Current | 2.0 Amp | • |
| 8 | DFP | Non-Contract Voice-Coil Actuators | Current Drive Bandwidth | 6 Hz | • 0-dB loop cross-over |
| 9 | DFP | Non-Contract Voice-Coil Actuators | Current Drive Noise | 180 nA/sqrt(Hz) | • One-sided noise spectral density |
| 10 | DFP | Non-Contract Voice-Coil Actuators | D/A Quantization | 61 uAmp/bit | • Least-Significant Bit; 16-bit D/A |
| 11 | DFP | Non-Contact Relative Position | Range | +/-12 mm | • Increases at lower relative pose control bandwidth for given slew agility |
| 12 | DFP | Non-Contact Relative Position | Noise | 16.38 nm/sqrt(Hz) | • Resolution: 366 nm over 500-Hz bandwidth |
| 13 | DFP | Non-Contact Relative Position | A/D Quantization | 366 nm/bit | • Least-Significant Bit; 16-bit A/D |
| 14 | DFP | Non-Contact Relative Position | Bandwidth | 30 kHz | • |
| 15 | DFP | Control System | Digital Logic Update Rate | 1 kHz | • |
| 16 | DFP | Control System | Payload Inertial Attitude Control Bandwidth | 0.584 Hz | • 0-dB loop cross-over; Gain Margin >11.2 dB; Phase Margin >57.6 deg |
| 17 | DFP | Control System | Spacecraft/Payload Relative Position Control Bandwidth | 0.11 Hz | • 0-dB loop cross-over; Gain Margin >11.6 dB; Phase Margin >92.6 deg |
| 18 | DFP | Control System | Spacecraft/Payload Relative Attitude Control Bandwidth | 7.7 mHz | • 0-dB loop cross-over; Gain Margin >9.6 dB; Phase Margin >72.6 deg |
| 19 | DFP | Control System | Spacecraft/Payload Relative Pose Estimator Bandwidth | 0.2 Hz | • -3-dB point |
| 20 | DFP | Control System | Gain Stabilization Filters | 1.0 Hz | • Second-order low-pass filter poles natural frequency (+ notch filters not listed) |
| 1 | Interface Cable | | Coupled System Natural Frequency | 3.5 to 257 mHz | • Based on Spacecraft and Payload rigid-body mass properties |
| 2 | Interface Cable | | Effective Linear Stiffness | 8.75 N/mm | • 50 lbf/in |
| 3 | Interface Cable | | Effective Rotational Stiffness | 1.97 N*m/deg | • 17.45 lbf-in/deg |
| 4 | Interface Cable | | Viscous Damping Cut-Off Frequency | 10*Fn | • Modeling intended to acknowledge dominantly position-dependent (friction) nature of damping in cables<br>• 10 x coupled system natural frequencies |
| 1 | Spacecraft | Reaction Wheels | Number Of Units | 8 | • Single axis Honeywell HR18-250: 3300 rpm nominal; Pyramid configuration |
| 2 | Spacecraft | Reaction Wheels | Peak Torque | 0.2 N-m | • Each unit; Up to 6000 rpm |
| 3 | Spacecraft | Reaction Wheels | Max Angular Momentum | 250 N-m-sec | • Each unit |
| 4 | Spacecraft | Reaction Wheels | Vibration Isolation System | 4 Hz; Q=10 | • [Option] Natural frequency and amplification at resonance; Notional |
| 5 | Spacecraft | | Attitude Control Bandwidth | 3.84 mHz | • Mode 1: Inertial attitude; Attitude Control System unused in Mode 3 |
| 6 | Spacecraft | | Fundamental Structural Natural Frequency | 0.048 Hz | • Sunshield mode |
| 1 | Payload | Fine Steering Mirror | Mirror Clear Aperture Diameter | 23 cm | • Versus ~14 cm required |
| 2 | Payload | Fine Steering Mirror | Operational Range | +/-0.22 deg | • Mechanical angle; Travel range: +/-0.25 deg |
| 3 | Payload | Fine Steering Mirror | Tip/Tilt Control Bandwidth | 50 Hz | • Inner loop on local relative position sensor: closed-loop -3 dB |
| 4 | Payload | Fine Steering Mirror | Actuator Current Drive Noise | 180 nA/sqrt(Hz) | • Actuator force constant 6 N/Amp; One-sided noise spectral density |
| 5 | Payload | Fine Steering Mirror | Actuator Command Quantization | 61 uA/bit | • Least-Significant Bit; 16-bit D/A |
| 6 | Payload | Fine Steering Mirror | Relative Position Sensor Noise | 1.5 nrad/sqrt(Hz) | • [Option] Zero in steady-state observation to mimic feedback on HDI (no inner loop)<br>• 18 bit effective resolution over 500 Hz and +/-0.25 deg travel range |
| 7 | Payload | Fine Steering Mirror | Line-Of-Sight Control Bandwidth | 2.0 Hz | • Outer loop: 0-dB loop cross-over; Type-II logic |
| 8 | Payload | | Fundamental Structural Natural Frequency | 10.67 Hz | • Secondary mirror tower |
| 9 | Payload | | Compliance in load path from DFP interface to telescope | 9.0 Hz | • First transmission zero<br>• Becomes design driver at frequencies below 1 Hz |

**Table 6** Payload Attitude Determination System Configuration.

| Sensor | | Sensor Parameter | EAC1 Configuration Value |
|---|---|---|---|
| Fine Guidance Sensor (FGS) | | Number of Units | 2 |
| | ■ | Boresight Angular Separation | 0.6-deg |
| | | Field Of View | 3 arcmin x 3 arcmin |
| | | Number of Sense Axes/each | 2 (tip/tilt) |
| | ■ | Noise Equivalent Angle (random error) | 3 mas (1 σ)<br>18-magnitude guide star<br>at 20-Hz update rate |
| | | Update Rate | 20 Hz |
| | | Synchronous Operation | Yes |
| Star Tracker (ST) | | Number Of Units | 3 |
| | | Geometric Configuration | Orthogonal Triad |
| | | Field Of View | 8-deg x 8-deg |
| | | Number of Sense Axes/each | 3 |
| | ■ | Noise Equivalent Angle (random error) | Tip/Tilt: 2.6 arcsec (1 σ)<br>Roll: 26 arcsec (1 σ) (TBV) |
| | | Max Slew Rate | Up to 2 deg/sec (TBV) |
| | | Update Rate | 10 Hz |
| | | Synchronous Operation | Yes |
| Inertial Reference Unit (IRU) | | Number Of Units | One Internally Redundant |
| | | Number of Sense Axes | 3 nominally orthogonal |
| | | Angle Random Walk | 0.019 arcsec/sec^(1/2) |
| | | Rate Random Walk | 1.33e-5 arcsec/sec^(3/2) |
| | | Bias Instability | 0.001 arcsec/sec |
| | | Gyro Bandwidth | 4 Hz |
| | | Quantization | 0.02 arcsec |
| | | Update Rate | 200 Hz |
| | | A/D Resolution | 16 bit |

As part of the process to evaluate whether EAC1 possesses the necessary attributes to achieve the telescope ultra-stability required for exoplanet imaging, we define a Design Departure Point. That process involves setting a set of configuration parameters covering the Disturbance Free Payload System, the power cable at the interface between the spacecraft and the payload, the spacecraft reaction-wheel assembly, and the Fast-Steering Mirror for line-of-sight stabilization among others. These configuration parameters are summarized in Table 5 and Table 6. In Table 5, the parameter values represent the results of sizing; trade analyses; and control system error rejection and stability analyses. Black boxes in those tables flag parameters, which are particularly critical to dynamic line-of-sight stability, dynamic wavefront stability, and slew agility performance; while grey boxes flag parameters, which are not yet included in our integrated model.

As reflected in the use of the term "Design Departure Point", our performance sensitivity analyses use those design parameters as nominal values.

### *4.3 Disturbance Free Payload System: Projected Telescope Performance Stability and Slew Agility*

#### *4.3.1 Spacecraft vibration mitigation performance projections*

**Vibration Transmissibility from Spacecraft to Payload**

Figure 19 shows the transmissibility of the spacecraft vibrations to the payload. That transmissibility is referenced to the Payload center of mass as necessary to properly assess coupling from spacecraft linear velocity to payload angular velocity, the rotation degrees of freedom being the most critical ones as far as the payload pointing is concerned. Figure 19 contains two sets of curves. The green set of curves corresponds to the case where the spacecraft and the payload are treated as perfect rigid-bodies. The blue set of curves corresponds to the case where the spacecraft and the payload flexible body dynamics are included.

The upper two quadrants show that the coupled system modes at frequencies around 80 mHz after cable stiffness compensation are well damped with a Q of less than 2. The break in the transmissibility curve around 1 Hz in those quadrants is due to a second-order roll-off filter used for gain stabilization in the DFP relative pose control logic.

The lower two quadrants corresponding to transmissibility to payload angular velocity are the two most important ones from a payload pointing stability performance perspective. The curves in the lower right quadrant show that the disturbance rejection is limited by the stiffness of the cable harness at frequencies above 0.1 Hz. The worst-case disturbance rejection is 16 dB at 0.11 Hz. The DFP system achieves 30 dB of disturbance rejection at 1 Hz and typically 60-dB of disturbance rejection or more at frequencies above 5 Hz. The residual transmitted vibrations are amplified by the payload structural dynamics at frequencies above 10 Hz. The effect of the Payload inertial attitude pointing control logic with a 0.58-Hz-bandwidth 0-dB cross-over including the associated integral control action is visible at frequencies below 1 Hz. That control logic achieves 60-dB or more of disturbance rejection below 17 mHz. The impact of the voice-coil actuator back-emf on the transmissibility is visible at the high-frequency end of the graph in the lower right quadrant: that effect is about a factor of 10 below the transmissibility due to the interface cable. As the transmissibility due to the cable increases the benefits of using a high-bandwidth current drive to reject the back-emf effects in the actuator diminish. On EAC1, we opted to reduce the actuator current drive bandwidth to 6-Hz 0-dB cross-over, which is sufficient to support a payload attitude control bandwidth of about 0.6-Hz, thereby reducing the effective actuation noise bandwidth.

Readers might notice that the rigid-body and flexible-body curves should track and not reverse trend at frequencies below 10 mHz. We traced these artifacts to numerical accuracy limitations in Matlab linearization tools when applied to multi-rate mixed discrete-continuous models.

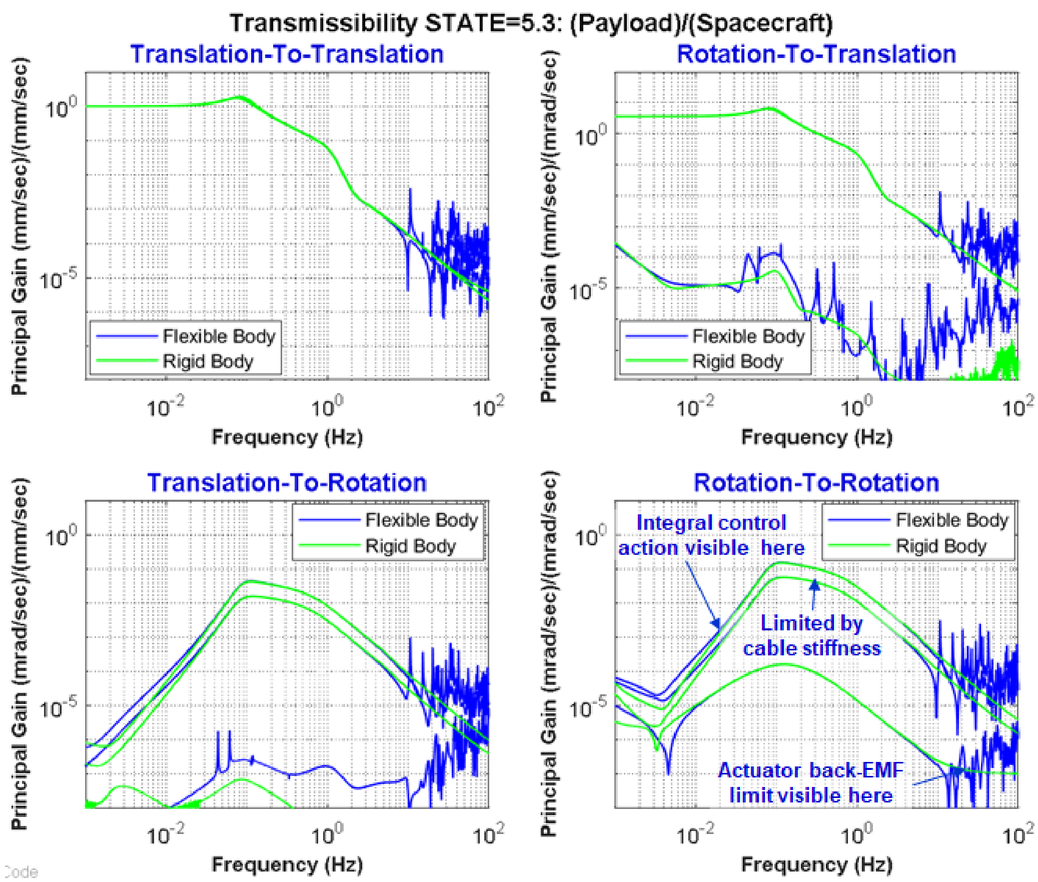


**Fig. 19** Rigid-body and flexible-body spacecraft disturbance transmissibility.

## Vibration Transmissibility from Spacecraft To Payload Dynamic Line Of Sight Error

Figure 20 shows the transmissibility of the spacecraft vibrations to the telescope optical line-of-sight. Figure 20 contains two sets of curves. The green set of curves captures the payload inertial angular velocity in response to the spacecraft inertial linear velocity (left graph) and angular velocity (right graph). The blue set of curves captures the payload inertial optical line-of-sight in response to spacecraft change in inertial position (left graph) and change in inertial orientation (right graph). The spacecraft linear and angular excitation is referenced to a point "fixed" in the spacecraft nominally coincident with the payload center of mass. The line-of-sight shown is after stabilization using a Fast-Steering-Mirror (FSM) in the coronagraph optical train with a 2-Hz control bandwidth 0-dB cross-over. In the frequence region below 10-Hz where the payload behaves dominantly as a rigid-body, the change in optical line-of-sight being a component of the change in orientation of the Payload in the absence of any inertial line-of-sight control, comparison between the green and the blue sets of curves gives a sense of the line-of-sight error rejection achieved by the Fast-Steering-Mirror control system.

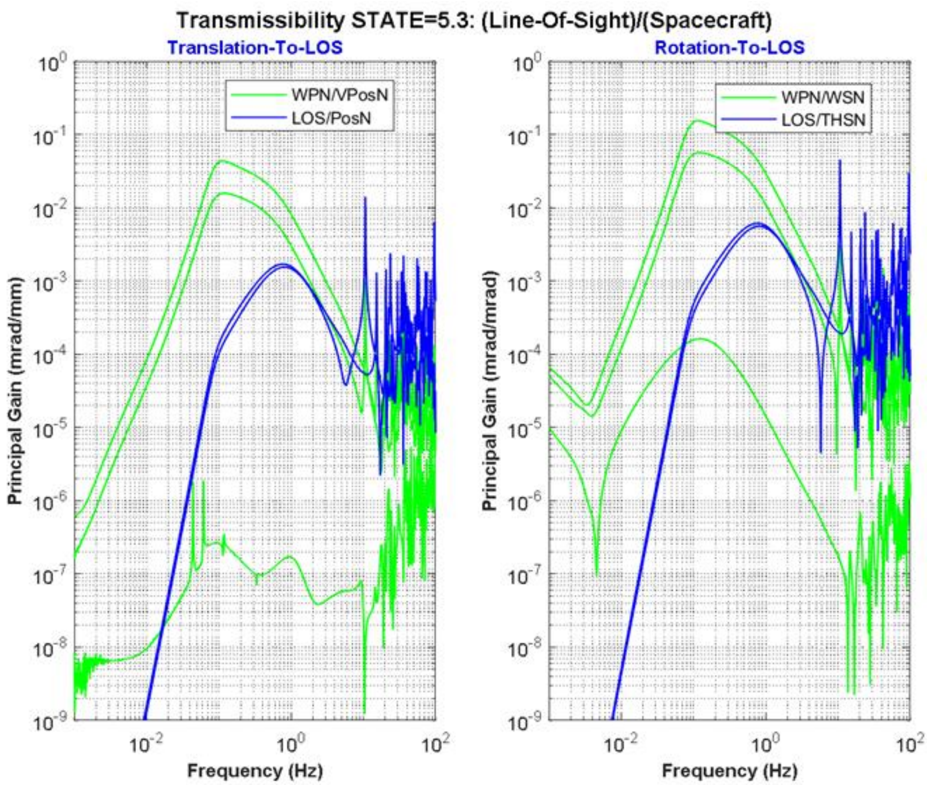


**Fig. 20** Transmissibility from Spacecraft Vibration to Dynamic Line Of Sight Error.

The graph shows that the Fast-Steering Mirror achieves 40-dB or more error rejection at frequencies below 0.1 Hz. At frequencies above 10 Hz, the line-of-sight error no longer follows the rigid-body trends due to the EAC1 payload internal structural resonances. The peak in the optical line of sight error response is at the secondary mirror tower mode resonance slightly above 10 Hz. In combination (right graph), the FSM inertial optical line-of-sight stabilization and the DFP vibration isolation and payload inertial attitude control system typically achieve 44-dB disturbance rejection below 100 Hz.

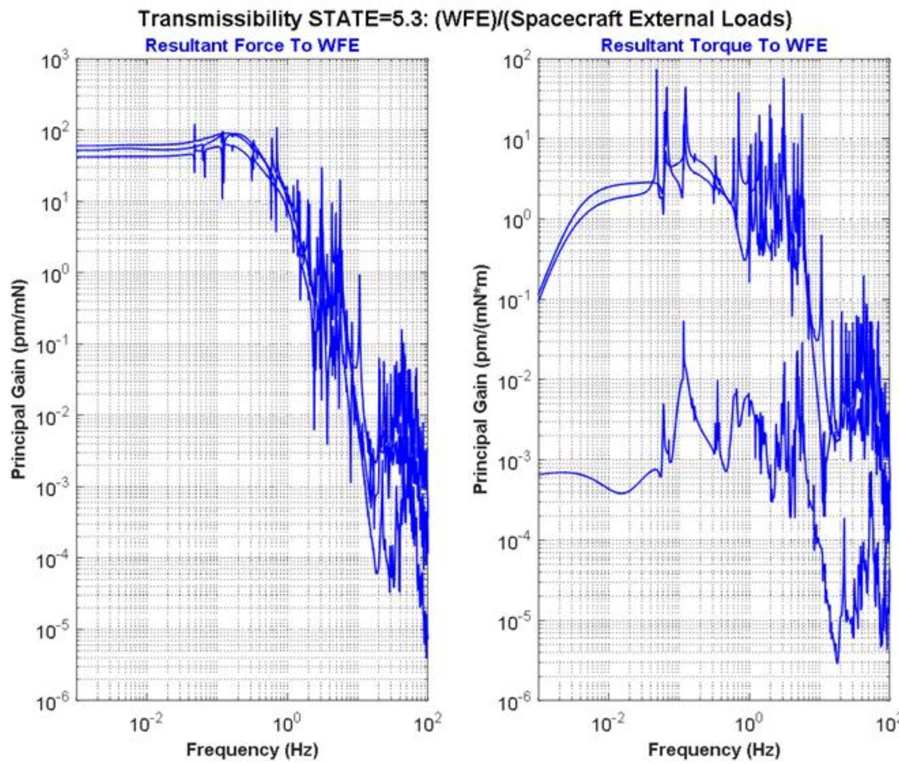


**Fig. 21** Transmissibility from Spacecraft External Loads to Dynamic Wavefront Error.

**Transmissibility from Spacecraft External Loads To Payload Dynamic Wavefront Error**

Figure 21 shows the transmissibility from external forces (left graph) and external torques (right graph) applied to the spacecraft to the dynamic wavefront error in one of the coronagraph instrument visible channels. While the observatory inertial attitude is under control during science observation, the observatory inertial position is not. When a constant external force acts on the spacecraft the entire observatory acquires a constant inertial acceleration. The left graph in Figure 21 shows that the deflections in the optical system under such quasi-static inertial linear accelerations result in wavefront errors in the range of 40 to (60 pm)/(mN).

The transmissibility from external forces and torques acting on the spacecraft to the dynamic wavefront errors is typically up to (100 pm)/(mN) and up to (70 pm)/(mN-m). The fundamental structural natural frequency of the payload being about 10 Hz, the graphs show that the spacecraft appendage modes poke through the Disturbance Free Payload interface below 5 Hz. These results also give a rough sense of the maximum allowable exported loads, should cryocoolers be used for detector cooling.

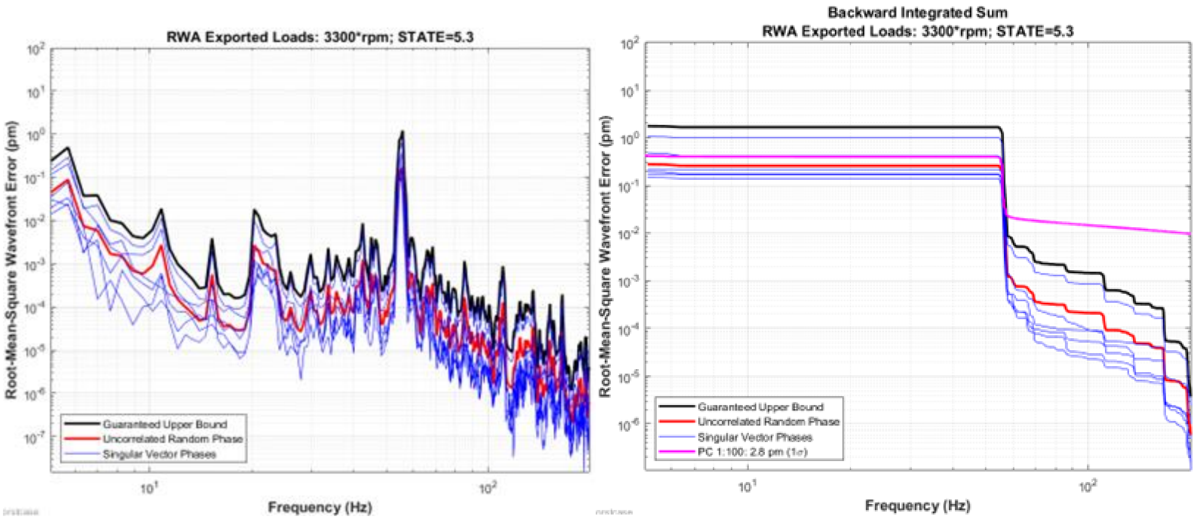


**Fig. 22** Transmissibility from Spacecraft Reaction-Wheel Exported Loads to Dynamic Wavefront Error.

**Dynamic Wavefront Error Due To Reaction-Wheel Assembly Exported Loads Alone: Worst Case Uncertainty Analysis**

Figure 22 shows the spatial root-mean-square dynamic wavefront error in one of the coronagraph instrument visible channels in response to forces and torques exported by hard-mounted reaction-wheels (left graph) and the associated backward integrated sum versus frequency (right graph). Our analyses are based on proprietary waterfall experimental data from Honeywell on its HR18-250 reaction-wheels. The data Honeywell provided are in the form of Fourier coefficient magnitude at wheels speeds ranging from 6000 rpm to 0 rpm in 30-rpm increments. In this analysis, all 8 wheels in the cluster are set to 3330 rpm (55.5 Hz) leading to excitation in a frequency region of high payload structural dynamics response due the rigid-body modes of the telescope primary mirror segments on their support structure.

The phase randomization process often used to convert from Fourier magnitude coefficients to forces and torques time-series for time simulation purposes leads to exported loads uncorrelated across degrees of freedom and across frequency bands around tones. While customary, that process is not well adapted because reaction-wheel exported loads are tonal in nature and highly correlated across degrees of freedom and in frequency bands around tones due to the dominant vibration sources being mass imbalance and bearing runout/rumble at nearly constant spin rate. A question that often comes up is: how much worse could the system responses possibly be for other phasing?

We implemented an alternate method in the frequency domain to analyze the dynamic wavefront error in response to the reaction-wheel exported loads based on principal gain analysis.

That method provides a guaranteed upper bound on the dynamic wavefront error regardless of phasing and it also provides phase realizations across degrees of freedom approaching that upper bound.

Figure 22 shows the difference in dynamic wavefront error as function of frequency depending on whether the phase is uncorrelated (red curve) or correlated across degrees of freedom. The black curve is the theoretical upper bound on the error for any phasing, which shows that the dynamic wavefront error could potentially be up to 4 to 5 times worse than by randomizing phases. The blue curves are example worst to best phase realizations based on principal vectors across 6 resultant forces and torques degrees of freedom. Those realizations bracket the randomized case as expected. They also show that our theoretical upper bound is only conservative by a factor of 1.5 to 2. The backward integrated dynamic wavefront error above 5 Hz is about 0.4 pm when randomizing the phase and about 1.1 pm for the worst-case phase realization based on the maximum principal vector. The dynamic wavefront error result in the randomized case matches the one we obtained in time domain simulations as expected when the reaction wheel exported loads are the sole source of disturbance.

#### *4.3.2 Dynamic line-of-sight and wavefront error steady-state performance projections following recentering maneuver*

In Figure 23, we provide time simulation results to evaluate the dynamic line-of-sight and the dynamic wavefront error performance of the DFP vibration isolation and precision pointing system and the line-of-sight stabilization system once steady state is reached following a recentering maneuver. The simulation demonstrates quick settling back into steady-state operating conditions following such maneuver—an off-nominal condition. Under DFP nominal operating conditions, recentering would happen gradually without inducing any dynamic transient.

In this simulation, as in the frequency domain analysis discussed earlier, all 8 wheels in the cluster are set to 3330 rpm (55.5 Hz) leading to excitation in a frequency region of high payload structural dynamics response due to the rigid-body modes of the telescope primary mirror segments on their support structure. All 8 wheels are hard-mounted, and the phases are randomized. The DFP relative pose and payload inertial attitude functions are all enabled. The Fast-Steering-Mirror line-of-sight stabilization control is enabled. Sources of noise include the DFP voice-coil actuator drive, the DFP relative position sensors, the Fast-Steering-Mirror actuator drive & local position sensors, and the Payload Attitude Determination System sensors. The Fast-Steering Mirror implementation presumes line-of-sight sensing will be available in the coronagraph instrument for line-of-sight control: the associated sensing noise is not modeled. The relative pose between the spacecraft and the payload starts offset from the desired set point with a relative position error of [0.1,0.2,0.3] mm and a relative attitude error (Body321 Euler angles) of [0.3,0.2,0.1]*deg. The start away from the desired set point causes a recentering maneuver at the beginning of the time simulation. The optical telescope does not include an active alignment system yet: designing and incorporating that system into our integrated modeling infrastructure is one of our next steps.

The lower left graph in Figure 23 shows that the inertial line-of-sight settles and reaches steady state within 5 seconds consistently with the 2-Hz Fast-Steering-Mirror control bandwidth. The upper left graph shows the dynamic line-of-sight errors over the last 200-seconds of the 500-sec simulation run. The steady-state dynamic line-of-sight errors are 216 and 220 uarcsec (1 $\sigma$) as compared to a desired goal of 300 uarcsec (1 $\sigma$). We confirmed by spectral analysis that the line-of-sight error is broadband not tonal in nature.

The upper right graph in Figure 23 shows the spatial root-mean-square dynamic wavefront error as function of time over the last 200-seconds of the 500-sec simulation run. We partitioned the dynamics wavefront error into a high- and a low-temporal component using 5-Hz as the boundary between the two. Frequencies above 5-Hz include the entirety of the payload structural dynamics on EAC1, the payload fundamental mode being about 10 Hz. Since the bandwidth of segment alignment control systems is typically limited to 1/5 to 1/10 of the payload fundamental natural frequency due to control-structure interaction, we anticipate most of the dynamic wavefront errors above 5-Hz will remain uncorrected. The dynamic wavefront error is 6.43 pm (1 $\sigma$) above 5-Hz and 4.47 pm (1 $\sigma$) below 5 Hz. Of the dynamic wavefront errors above 5 Hz, a separate simulation configured to operate Payload attitude control on truth attitude shows that all the sources of errors other than the ADS account for 0.57 pm (1 $\sigma$) indicating that the ADS sensors noise dominates the wavefront error at the 10:1 level.

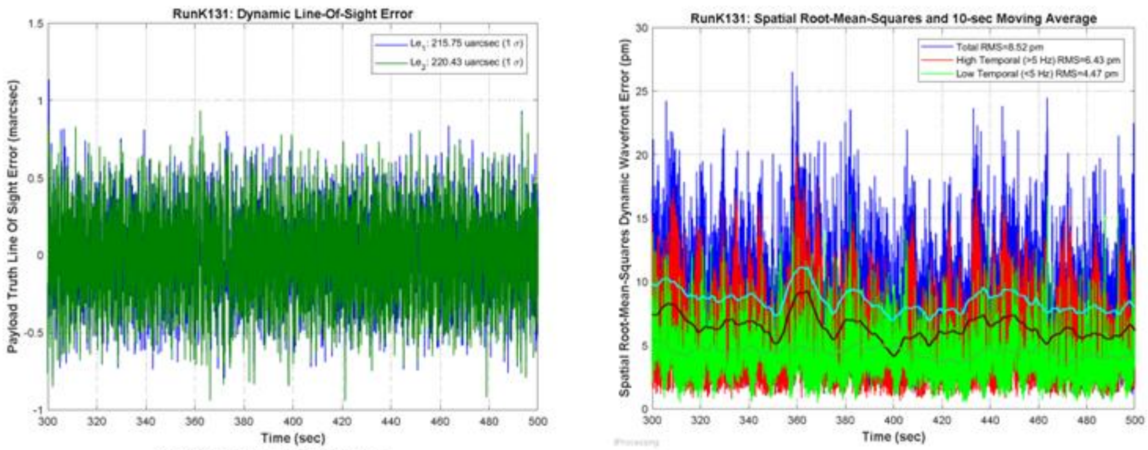


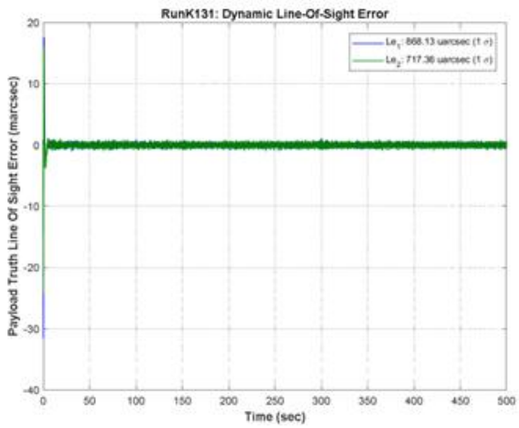


| Line-Of-Sight Error Instability over last 200 sec (micro-arcsec 1 σ) | | Dynamic Wavefront Error over 10 sec (pm 1 σ) | |
|---|---|---|---|
| L1 | L2 | <5 Hz | >5 Hz |
| 216 | 220 | 4.47 | 6.43 |

**Fig. 23** EAC1 Steady-State Dynamic Optical Stability Performance.

Figure 24 shows the principal gains of the spectrum of the dynamic wavefront error (left plot) and the associated backward sum as a function of frequency (right plot). The backward integrated dynamic wavefront error above 5 Hz of 7.3 pm (1 σ) in this spectral analysis is roughly consistent with the 6.43 pm (1 σ) reported earlier obtained in the time domain. Most of the power is in the telescope secondary mirror tower mode near 10 Hz. Interestingly, while the wavefront has many more degrees of freedom than shown in the left graphic, our principal component analysis shows that only 6 principal components participate significantly in the response, all the others (not shown) are multiple orders of magnitude smaller. That is attributable to the number of inputs in the system: in particular, there are only 6 possible degrees of freedom at the interface that can contribute to the transmissibility from the spacecraft to the payload, and DFP Payload-attitude control.

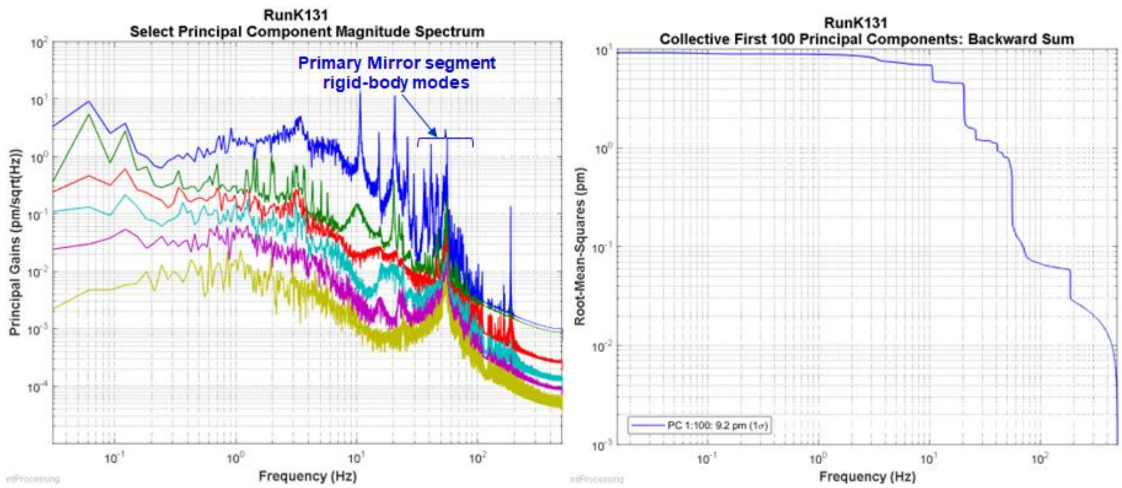


**Fig. 24** EAC1 Steady-State Dynamic Wavefront Error Performance.

Figure 25 shows the Extended Kalman Filter Payload Attitude Determination System performance over the last 200 sec of the 500 sec simulation: the Payload attitude reconstruction errors are 1.0 marcsec (1 σ) in the tip and tilt axes, and 3.4 marcsec (1 σ) in the roll axis. The reconstruction errors are larger in the roll-axis due to the small angular separation (0.6-deg) between the two Fine Guidance Sensor boresights.

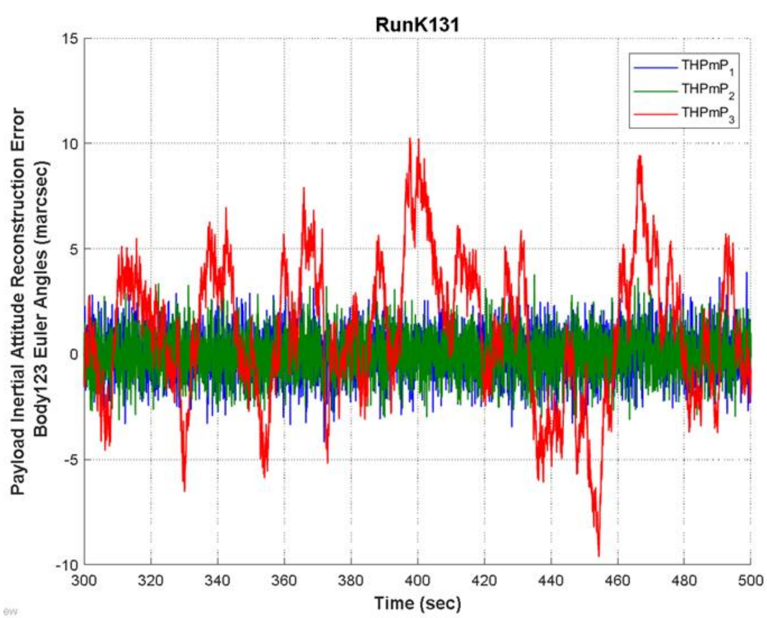


**Fig. 25** Payload Attitude Determination System Performance: Payload Attitude Reconstruction Error.

Figure 26 shows the steady-state Payload inertial attitude control error over the last 200 sec of the 500 sec simulation: the Payload attitude control errors are 2.1 marcsec (1 σ) in the tip axis, 1.6 marcsec (1 σ) in the tilt axis, and 4.3 marcsec (1 σ) in the roll axis. The control errors are larger in the roll-axis due to the payload attitude knowledge errors being worse in that axis.

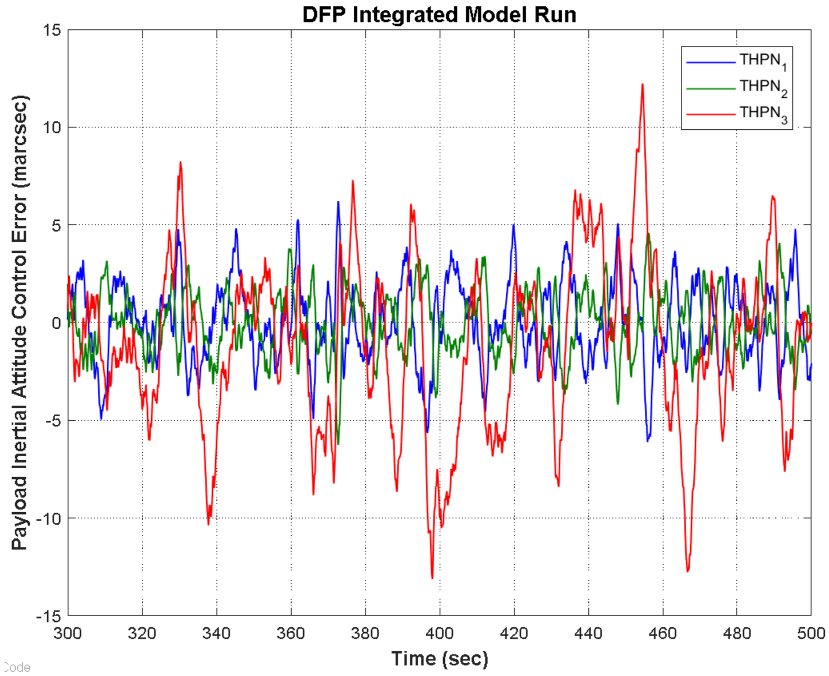


**Fig. 26** Steady-State Payload Attitude Control Error.

*4.3.3 Coordinated large angle slew agility*

In this section, we now present the results of a large angle slew time simulation demonstrating coordinated spacecraft/DFP/payload operations achieving the observatory slew agility objectives. For reference, the observatory field of regard is +/-45-deg and the agility objective is to slew the observatory by 90-deg in less than 60-minutes over the field of regard corner-to-corner. The maximum projected slew angle between the reference star for digging the dark hole and the target star for science observation is 30-deg. Our slew scenario here is commensurate with those general observatory objectives and is as follows.

We initialize the payload in the [0;0;0] deg start inertial orientation and set the Body321 Euler angles for the payload terminal inertial orientation to [30;20;10]-deg corresponding to a total slew angle of ~37.4-deg. The objective is to slew the payload from the start to the terminal orientation in 38 minutes and then transition the payload to non-zero terminal inertial angular rates of [-3;-2;-1] mdeg/sec as may be required to track a target for instance. We intentionally offset the initial pose between the spacecraft and the payload from the desired set point so that DFP is near the end of its operating range to demonstrate that DFP can successfully execute slews starting from off-nominal conditions: we set the relative position error to [0.1;0.2;0.3] mm and the relative attitude error (Body321 Euler angles) to [0.3;0.2;0.1]*deg. The peak DFP relative position sensor output is then -8.3-mm out of the +/-12-mm available range. The DFP system coordinates its operations with the spacecraft and the payload to bring the DFP system back near the middle of its operating range while executing the slew. In this simulation, DFP acts as the Master, but the DFP software is configurable so that either the payload or the spacecraft could also act as the Master for coordinating the slew operations, if desired.

The observatory model in this slew simulation is configured as described in Table 5 per the design departure point and Table 6 for the payload Attitude Determination system. In particular, the DFP payload inertial attitude control bandwidth is set to 0.58-Hz allowing tight payload attitude control; the payload Line-Of-Sight control is enabled throughout, and the Fast-Steering Mirror control bandwidth (outer loop) is set to 2 Hz. Our integrated model simulation includes the payload and the spacecraft flexible-body dynamics. Payload inertial attitude control operates on the ADS star trackers and IRU during the slew and transitions to operation on the ADS Fine Guidance Sensors and IRU upon completion of the slew (we do not simulate/respect the details of the Fine Guidance Sensors target tracking rate limitations, or star Identification and Acquisition periods at the end of the slew, which last less than 145 sec combined).[48] To avoid creating transients, the DFP slew generation code sets the specified payload inertial attitude to the current payload inertial attitude as reported by the ADS at the start of the slew and shapes the slew profile at both the start and the end of the slew.

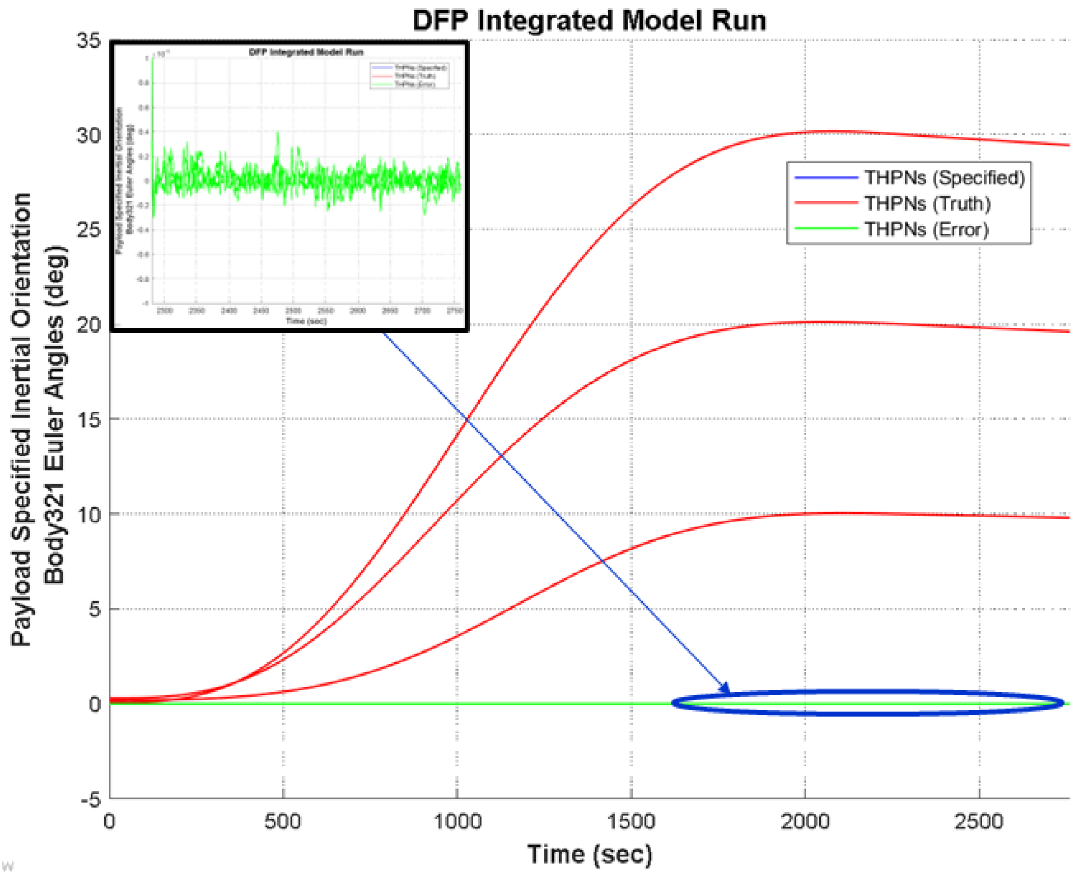


**Fig. 27** Coordinated Large Angle Slew with Spacecraft and Payload Flexible Body Dynamics.

Figure 27 shows the results of our slew simulation. Figure 27 contains three sets of curves: the red set of curves corresponds to the truth payload inertial attitude trajectory; the blue set of curves corresponds to the specified payload inertial attitude slew profile (visually indistinguishable from the truth); and the green set of curves corresponds to the payload inertial attitude control error. The insert in that figure zooms on the payload inertial attitude control error near and past the end of the slew. The payload inertial attitude control error is less than 5.1 urad during slew, less than 8.1 marcsec (1 $\sigma$) past the end of the slew, and less than 3.6 marcsec (1 $\sigma$) 330 sec past the end of the slew (indicating fully settled conditions). That attitude error is generally consistent with the Fine Guidance Sensor noise equivalent angle of 3 marcsec over its 10-Hz Nyquist bandwidth.

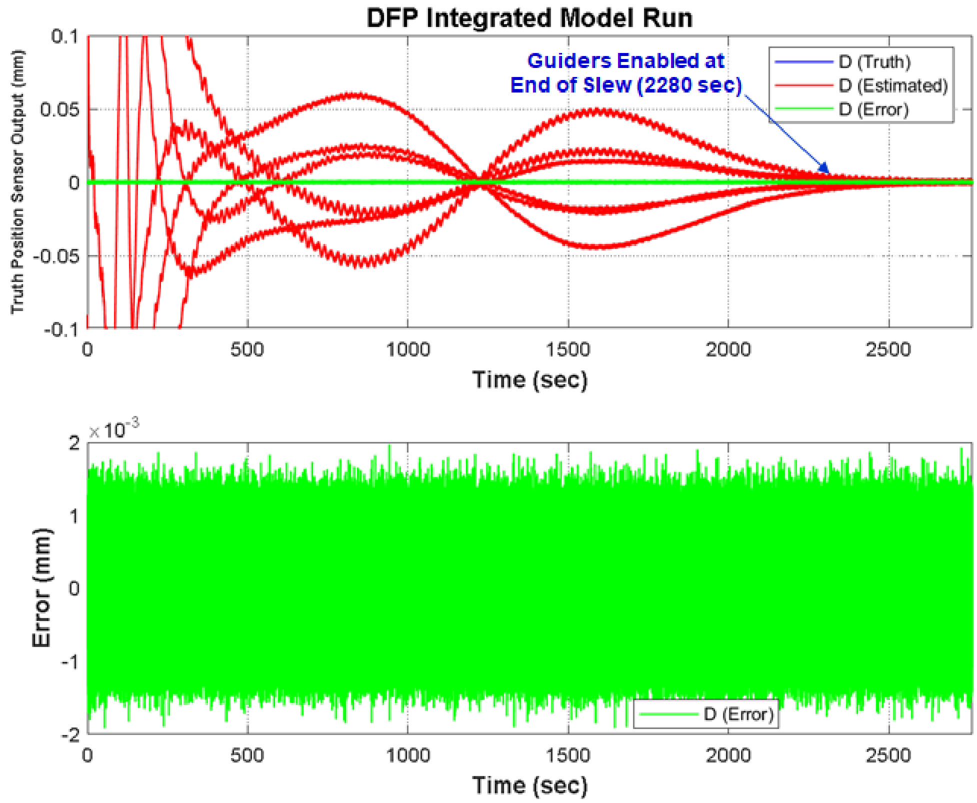


**Fig. 28** Past Recentering Maneuver, Sensing Range Required of Relative Position Sensors to Execute Slew is Less Than 0.1 mm Out of +/-12-mm Available Range

Figure 28 shows the range required from all six DFP non-contact inductive position sensors arranged in a regular hexapod configuration and used to monitor the relative pose between the payload and the spacecraft. That figure compares the truth (blue) and reconstructed (red) position sensor outputs; the green set of curves shows the reconstruction errors. Our simulation includes detailed models of the DFP relative position sensors anchored in experimental data and the reconstruction is based on look-up tables to invert the sensor non-linearity. Figure 28 shows that DFP gracefully recenters the relative pose between the payload and the spacecraft during the slew. The peak relative position sensor output is -8.3 mm out of the +/-12-mm available range due to specified initial conditions as indicated in the slew scenario description. Had the slew been started in the middle of the DFP operating range, the relative position range required to execute slew would have been <0.1 mm. The lower half of Figure 28 shows that the sensor non-linearity is well inverted: the position sensor residual systematic errors are significantly below the random errors of 0.38 um (1 σ).

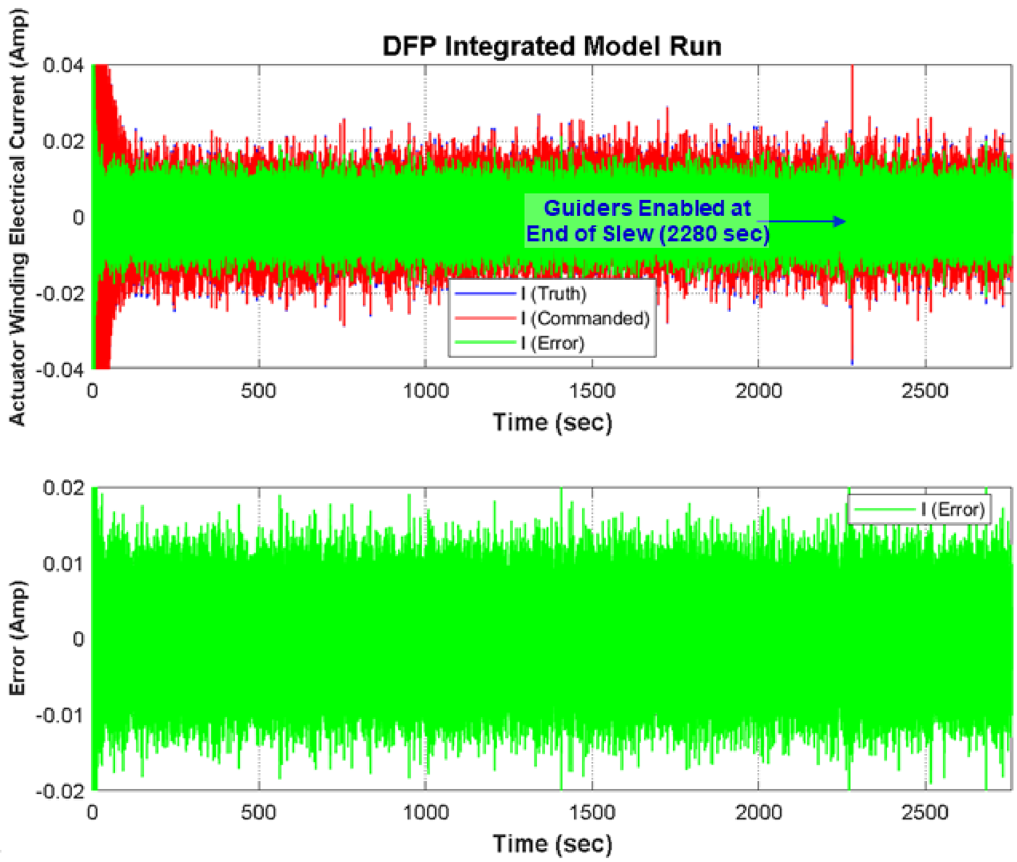


**Fig. 29** Past Recentering Maneuver, Winding Current Required of Non-Contact Voice-Coil Actuators to Execute Slew is Less Than 30 mA Out of +/-2 A Available Range.

Figure 29 shows the winding current required of all six DFP non-contact voice-coil actuators arranged in a regular hexapod configuration and used to control the inertial attitude of the payload. That figure compares the truth (blue) and commanded (red) actuator drive currents; the green set of curves shows the control errors. Our simulation includes detailed models of the DFP non-contract voice-coil actuators anchored in experimental data and the command is based on look-up tables to invert the actuator non-linearity. Figure 29 shows that DFP gracefully recenters the relative pose between the payload and the spacecraft during the slew. The peak actuator winding current is up to 0.8 A 0-to-peak out of the +/-2 A available range due to specified initial conditions as indicated in the slew scenario description. Had the slew started in the middle of the DFP operating range, the peak actuator winding current to execute the slew would have been < 30 mA. The lower half of Figure 29 shows that the actuator non-linearity is well inverted: the systematic control errors (not visible) are dominated by residual back-emf and are well below the random errors of 4.4 mA (1 $\sigma$) after 5 seconds.

In the next section, we present the dynamic line-of-sight and dynamic wavefront stability performance past the end of the slew just described achieved with the DFP system.

*4.3.4 Dynamic line-of-sight and wavefront error performance projection following large angle slews*

Figure 30 describes the dynamic line-of-sight and the dynamic wavefront error performance of the DFP vibration isolation and precision pointing system and the line-of-sight stabilization system past the end of the slew. All 8 spacecraft-reaction-wheels are hard-mounted, and the exported loads modeling is limited to static and dynamic imbalance. Accordingly, those exported loads vary consistently with the wheel speeds required to execute the slew. The optical telescope control model does not include an active alignment system yet: designing and incorporating that system into our integrated modeling infrastructure is one of our next steps.

The lower left graph in Figure 30 shows that the inertial line-of-sight settles and reaches steady state within a few seconds consistently with the 2-Hz Fast-Steering-Mirror control bandwidth. The upper left graph shows the dynamic line-of-sight errors over the last 200-seconds of the 46-minute simulation run. The steady-state dynamic line-of-sight errors are 223 and 229 uarcsec (1 $\sigma$) as compared to a desired goal of 300 uarcsec (1 $\sigma$). We confirmed by spectral analysis that the line-of-sight error is broadband not tonal in nature.

The upper right graph in Figure 30 shows the spatial root-mean-square dynamic wavefront error as function of time over the last 200-seconds of the slew simulation. We partitioned the dynamics wavefront error into a high- and a low-temporal component using 5-Hz as the boundary between the two. Frequencies above 5-Hz include the entirety of the payload structural dynamics on EAC1, the payload fundamental mode being about 10 Hz. Since the bandwidth of segment alignment control systems is typically limited to 1/5 to 1/10 of the payload fundamental natural frequency due to control-structure interaction, we anticipate that such feedback systems will leave most of the dynamic wavefront errors above 5-Hz uncorrected. The dynamic wavefront error is 6.34 pm (1 $\sigma$) above 5-Hz and 3.82 pm (1 $\sigma$) below 5 Hz. Of the dynamic wavefront errors above 5 Hz, a separate simulation configured to operate Payload attitude control on truth attitude shows that the ADS sensors noise dominates the wavefront error at the 10:1 level.

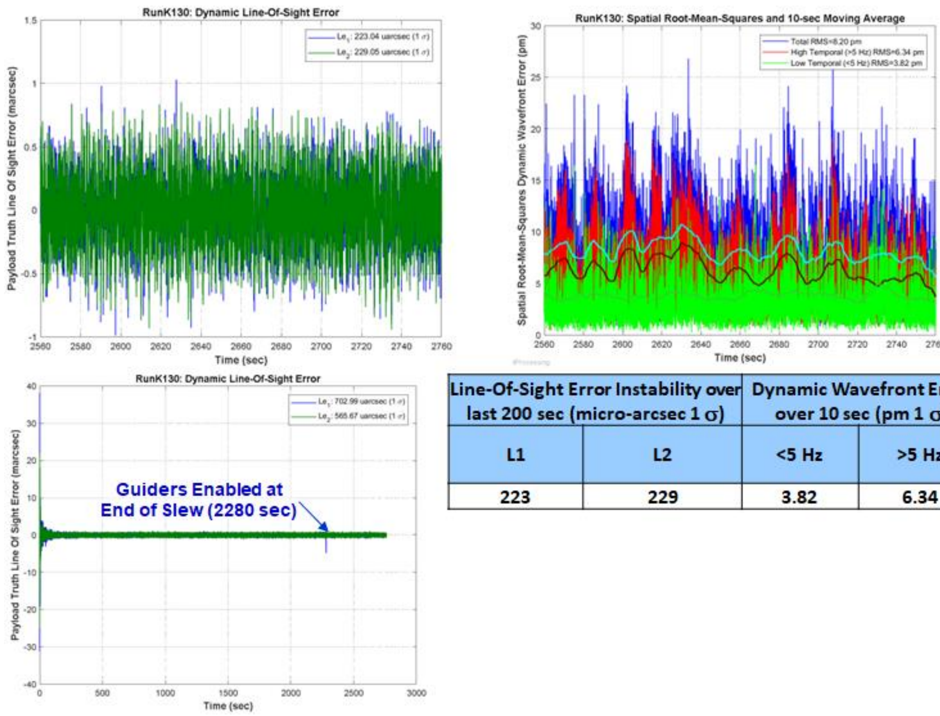


| Line-Of-Sight Error Instability over last 200 sec (micro-arcsec 1 σ) | | Dynamic Wavefront Error over 10 sec (pm 1 σ) | |
|---|---|---|---|
| L1 | L2 | <5 Hz | >5 Hz |
| 223 | 229 | 3.82 | 6.34 |

**Fig. 30** EAC1 Dynamic Optical Stability Performance Past End of Slew Achieved With DFP System.

Figure 31 shows the principal gains of the spectrum of the dynamic wavefront error (left plot) and the associated backward sum as a function of frequency (right plot). The backward integrated dynamic wavefront error of 7.2 pm (1 σ) above 5 Hz in this spectral analysis is generally consistent with the 6.3 pm (1 σ) reported in Figure 30 obtained in the time domain. Most of the power is in the telescope secondary mirror bending modes near 10 Hz. As pointed out earlier, interestingly, while the wavefront has many more degrees of freedom than shown in the left graphic, our principal component analysis shows that only 6 principal components participate significantly in the response, all the others (not shown) are multiple orders of magnitude smaller. That is attributable to the number of inputs in the system: in particular, there are only 6 possible degrees of freedom at the interface that can contribute to the transmissibility from the spacecraft to the payload.

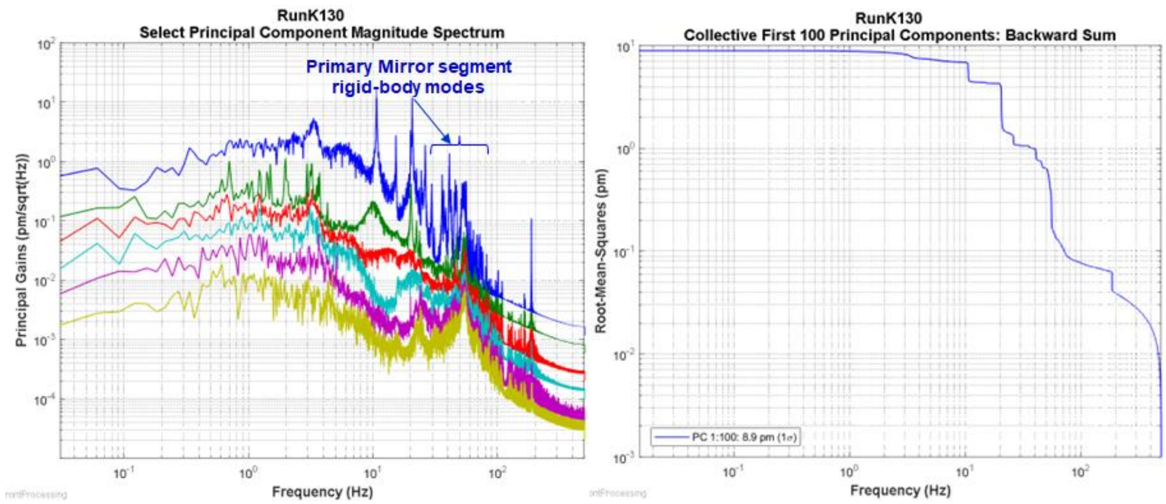


**Fig. 31** EAC1 Dynamic Wavefront Error Performance Past End of Slew Achieved With DFP System.

### *4.4 Bottoms Up Dynamic Line-Of-Sight and Dynamic Wavefront Error Budgets*

Table 7 and Table 8 present our projected dynamic line-of-sight and dynamic wavefront error bottoms up error budgets, respectively, specifically for EAC1.

**Table 7** Dynamic Line-Of-Sight Error Budget.

| Inertial Line-Of-Sight Instability: Goal: 300 uasec (1 σ) Per Axis | | | | | |
|---|---|---|---|---|---|
| | Error Source | | | Projected [uasec (1 σ)] | Comments/Assmptions |
| 1 | DFP | Voice-Coil Actuators | Current Drive Noise | 0.6 | • One-sided noise spectral density: (180 nA/sqrt(Hz)) [5 N/Amp force constant]<br>• Current drive bandwidth: 6-Hz (0-dB loop cross-over) |
| 2 | DFP | Voice-Coil Actuators | D/A Noise and Distortion | 0.3 | • Allocation; Least-Significant Bit: (61 uA/bit) Departure Point/4 |
| 3 | DFP | Relative Position Sensors | Noise | 4 | • One-sided noise spectral density: 16.38 nm/sqrt(Hz) |
| 4 | DFP | Relative Position Sensors | A/D Noise and Distortion | 4 | • Allocation; Least-Significant Bit: (366 nm/bit) |
| 5 | Spacecraft | Reaction-Wheels | | 7 | • Honeywell HR18-250 : 6000 rpm max<br>• Worst case phasing across excitation degrees-of-freedom at 3330 rpm<br>• Vibration isolation system: 4-Hz natural frequency; Q=10 |
| 6 | Spacecraft | Fuel Slosh | | 28 | • Allocation; >43-dB rejection below 1 Hz from DFP + FSM |
| 7 | Spacecraft | Spacecraft Attitude Control System Jitter | | 28 | • Allocation; >43-dB rejection below 1 Hz from DFP + FSM |
| 8 | Payload | Fine Steering Mirror | Actuator Current Drive Noise | 17 | • One-sided noise spectral density: 180 nA/sqrt(Hz) [6 N/Amp force constant] |
| 9 | Payload | Fine Steering Mirror | Actuator Command Noise and Distortion | 6 | • Least-Significant Bit: 61 uA/bit |
| 10 | Payload | Fine Steering Mirror | Relative Position Sensor | 125 | • Zero, if feedback on CI (no inner loop)<br>• One-sided noise spectral density: 11.91 nrad/sqrt(Hz) |
| 11 | Payload | Coronagraph Instrument (TBV) Noise | | 145 | • One-sided noise spectral density: 46*uasec/sqrt(Hz) in object space<br>• Pointing data update rate: 100 Hz |
| 12 | Payload | Attitude Determination System | | 229 | • DFP Payload inertial attitude control bandwidth: 0.58 Hz |
| 13 | Payload | Active Alignment System | | 50 | • Allocation<br>• Mirror segment alignment system; Secondary Mirror alignment system |
| 14 | | Margin/Uncertainty | | 170 | • |
| | | | Total (Root-Sum-Squares) | 350 | |

Black boxes in these tables flag error sources, which are performance drivers, while greyed out boxes flag error sources, which are budgeted but are not currently represented in our integrated models. Our error budgeting process involves first identifying and categorizing the sources of errors. Next, whenever an error source is represented in our integrated model, we run time simulations under steady-state observing conditions with that error source enabled while all the other sources of errors are disabled and then evaluate the dynamic line-of-sight and the dynamic wavefront error to isolate and quantify the contribution of that error source alone. Whenever an error source is not yet represented in our models, we enter an error allocation in the budget table based on available information such as vibration transmissibility in the case of spacecraft fuel slosh, or vendor datasheet specifications in the case of analog-to-digital and digital-to-analog converters distortion (integral non-linearity) for instance, or engineering judgement.

These tables represent dynamic line-of-sight and dynamic wavefront errors prior to any wavefront sensing and control compensation and might therefore best be termed “uncorrected”. These tables focus on the “dynamic”, not the “quasi-static” sources of errors such as dimensional instability over long time scale (~>10 sec) driven by changes in the operational thermal environment for instance.

Currently, our integrated models do not include an Active Alignment System to maintain the optical elements as rigid-bodies in the optical telescope assembly in their desired relative pose and keep the telescope phased: designing and incorporating that system into our integrated modeling infrastructure is an ongoing activity.

**Dynamic Line-Of-Sight Error Budget.** We are currently projecting 350-uarcsec (1 $\sigma$) dynamic line-of-sight errors including a 170-uarcsec (1 $\sigma$) uncertainty allocation. The Fast-Steering-Mirror relative position sensor noise, the coronagraph line-of-sight sensor noise, and the Attitude Determination System estimation errors are the dominant sources of errors. The dynamic line-of-sight errors due to spacecraft vibrations (reaction-wheels) and Disturbance Free Payload system are well-controlled. Margin would be desirable at this early stage, which may require a Fine Guidance Sensor noise-equivalent angle lower than the 3 masec (1 $\sigma$) over 10-Hz Nyquist bandwidth used in this study.

**Dynamic Wavefront Error Budget.** We currently project achieving less than 20 pm (1 $\sigma$) dynamic wavefront error above 5 Hz including a 10-pm uncertainty allocation. Understanding better whether that level of dynamic stability above 5-Hz is sufficient for exoplanet imaging is an ongoing activity. We used 5-Hz as frequency threshold because, as a feedback system, the Active

Alignment System will likely leave these dynamic wavefront errors uncorrected due to control-structure interaction limiting the achievable error rejection bandwidth of that system. The Attitude Determination System and the Active Alignment System (not modeled) are the dominant sources of errors. We allocated dynamic wavefront errors on the order of 10-pm to the Active Alignment System to account for a combination of picometer actuation noise, feedback of edge sensor and long-distance metrology noise, and dynamic interaction with the optical telescope assembly with that system. The dynamic wavefront errors above 5-Hz originating from spacecraft vibrations (reaction-wheels), the Disturbance Free Payload system, and the Fast-Steering Mirror are well-controlled (below the picometer-level individually). These positive results reflect our progress on reducing the DFP voice-coil actuator error contribution (by reducing current drive bandwidth) discussed in Section 3.1.2.

At frequencies below 5-Hz, we project less than 20 pm (1 $\sigma$) dynamic wavefront error including a 10-pm uncertainty allocation. As mentioned earlier, these are errors prior to any correction by the optical telescope assembly Active Alignment System. As is the case above 5-Hz, the dynamic wavefront errors below 5-Hz originating from spacecraft vibrations (reaction-wheels), the Disturbance Free Payload system, and the Fast-Steering Mirror are all well-controlled (typically below the picometer-level individually).

**Table 8** Dynamic Wavefront Error Budget.

| Dynamic Wavefront Error: Threshhold: 50 pm (1 σ); Goal: 10 pm (1 σ) | | | | | | | |
|---|---|---|---|---|---|---|---|
| Error Source | | | | | Projected [pm (1 σ)] <5 Hz | Projected [pm (1 σ)] >5 Hz | Comments/Assmptions |
| 1 | DFP | | Voice-Coil Actuators | Current Drive Noise | 0.1 | 0.5 | • One-sided noise spectral density: (180 nA/sqrt(Hz)) [5 N/Amp force constant]<br>• Current drive bandwidth: 6-Hz (0-dB loop cross-over) |
| 2 | DFP | | Voice-Coil Actuators | D/A Noise and Distortion | 2.0 | 1.0 | • Allocation; Least-Significant Bit: (61 uA/bit) Departure Point/4 |
| 3 | DFP | | Relative Position Sensors | Noise | 0.3 | 0.5 | • One-sided noise spectral density: 16.38 nm/sqrt(Hz) |
| 4 | DFP | | Relative Position Sensors | A/D Noise and Distortion | 0.3 | 0.5 | • Allocation; Least-Significant Bit: (366 nm/bit) |
| 5 | Spacecraft | | Reaction-Wheels | | 1.0 | 0.3 | • Honeywell HR18-250 : 6000 rpm max<br>• Worst case phasing across excitation degrees-of-freedom at 3330 rpm<br>• Vibration isolation system: 4-Hz natural frequency; Q=10 |
| 6 | Spacecraft | | Fuel Slosh | | 1.0 | 0.5 | • Allocation |
| 7 | Spacecraft | | Spacecraft Attitude Control System Jitter | | 1.0 | 0.5 | • Allocation |
| 8 | Payload | | Fine Steering Mirror | Actuator Current Drive Noise | 0.7 | 0.6 | • One-sided noise spectral density: 180 nA/sqrt(Hz) [6 N/Amp force constant] |
| 9 | Payload | | Fine Steering Mirror | Actuator Command Noise and Distortion | 0.2 | 0.2 | • Least-Significant Bit: 61 uA/bit |
| 10 | Payload | | Fine Steering Mirror | Relative Position Sensor Noise | 0.1 | 0.5 | • Zero, if feedback on CI (no inner loop)<br>• One-sided noise spectral density: 11.91 nrad/sqrt(Hz) |
| 11 | Payload | | Coronagraph Instrument (TBV) Noise | | 1.8 | 1.3 | • One-sided noise spectral density: 46*uasec/sqrt(Hz) in object space<br>• Pointing data update rate: 100 Hz |
| 12 | Payload | | Attitude Determination System | | 3.8 | 6.3 | • DFP Payload inertial attitude control bandwidth: 0.58 Hz |
| 13 | Payload | | Active Alignment System | | 10.0 | 10.0 | • Allocation<br>• Mirror segment alignment system; Secondary Mirror alignment system |
| 14 | | | Margin/Uncertainty | | 10.0 | 10.0 | • |
| | | | | Total (Root-Sum-Squares) | 15.0 | 15.6 | • Combined low & high: 22 pm (1 σ) |

# 5 Summary Evaluation Findings and Future Observatory Architecture Recommendations

## *5.1 EAC1 stiffer payload structure as compared to predecessor concepts LUVOIR-A and LUVOIR-B offers major benefits*

Our LUVOIR-B integrated modeling studies [Ref. 18] highlighted the performance limitations imposed by the optical telescope assembly low-frequency flexible-body dynamics on the achievable dynamic wavefront errors and on the achievable active alignment system control bandwidth due to control-structure interaction. To address these limitations, NASA and its partners designed Exploratory Analytical Case 1 to achieve significantly higher structural modal frequencies. The modal frequency of the secondary mirror tower was increased from 1.5 Hz on LUVOIR-B to 10.6 Hz on EAC1, and the modal frequencies of the primary mirror segment rigid-body modes on their support backplane structure were raised to above 40 Hz on EAC1. While additional design fidelity is required in the mechanical interfaces/joints to confirm whether such increased modal frequencies are indeed achievable, our EAC1 integrated modeling studies clearly demonstrate the benefits of aiming for optical telescope assembly structural modal frequencies above 10 Hz and we recommend continuing to aim for that objective in the future. Besides easing system integration and enabling functional testing of the optical telescope assembly in the laboratory prior to launch  (for reference, a 1.5-Hz structure would deflect by ~11-cm in 1-G without a gravity offload system), our EAC1 integrated modeling studies highlight the following benefits of having a stiffer payload, which cut across multiple subsystems including vibration isolation system between spacecraft and payload, reaction-wheel local vibration isolation, OTA active alignment system achievable control bandwidth, Fast Steering Mirror required bandwidth, wavefront sensing required update rate, need or not for structural damping augmentation, need or not for feedforward compensation:

(1) A stiffer payload translates into reduced sensitivity to residual exported loads past the vibration isolation system acting on the payload and affecting the dynamic wavefront errors above 5 Hz by a factor of about 5. Limiting dynamic wavefront errors above 5 Hz to allowable levels is essential as these errors will likely remain uncorrectable by active feedback control means due to control-structure interaction limiting the achievable active alignment control system bandwidth. Addressing excessive dynamic wavefront errors above 5 Hz would then require other mitigation measures such as structural damping augmentation, or mirror segment rigid-body-alignment feedforward compensation, with commensurate increase in system complexity to manage the optical telescope assembly dynamic dimensional stability.

(2) A stiffer payload structure allows accommodating stiffer power cables at the vibration isolation system interface between the spacecraft and the payload. On EAC1, we estimate the coupled system modal frequencies due to the power cable are up to 0.26-Hz. The increase in vibration transmissibility due to the electrical power cable on EAC1 remains manageable relative to the HWO dynamic wavefront error objectives of ~<10 pm (1 $\sigma$): dynamic wavefront errors due to hard-mounted reaction-wheels exported loads for instance are managed to below 1 pm (1 $\sigma$). Managing the interface cable would have been much more difficult had the payload structure been more compliant as in LUVOIR-B due to insufficient modal frequency separation between the suspension modes (0.26 Hz) and the optical telescope assembly fundamental mode (1.5 Hz).

(3) A stiffer payload structure allows achieving a higher payload attitude control bandwidth with the DFP system, which translates into tighter control of the payload line-of-sight and lower transmissibility of spacecraft low-frequency appendage mode vibrations as needed to deal with the increase in vibration transmissibility up to higher temporal frequencies from the

power cable. We were able to increase the payload attitude control bandwidth from 36.5 mHz on LUVOIR-B to 0.58-Hz on EAC1. In the payload attitude degrees of freedom, DFP acts as an inertial stabilization system at low frequencies (as opposed to a vibration isolation system). The higher the DFP payload inertial attitude control bandwidth, the higher the disturbance rejection at low frequencies (low meaning typically below 1 Hz). Those results are predicated on the payload coming with an Attitude Determination System with sufficient bandwidth for inertial attitude control: the JWST Fine Guidance Sensors with a 20-Hz update rate and Inertial Reference Unit with 4-Hz bandwidth and 200-Hz update rate are commensurate to achieving the target 0.58-Hz bandwidth just referenced during science observations.

(4) A stiffer payload structure allows dealing with large offsets (~3 m on EAC1) between the vibration isolation system location and the effective center of mass of the combined payload and spacecraft. That offset translates into increased transmissibility of spacecraft vibration to the payload due to coupling from spacecraft translation accelerations into payload rotation accelerations. That effect applies to any type of vibration isolation system. Without the addition of a sunshield as in JWST, such large offset will likely be an inherent characteristic of any future observatory layout due to the mass/inertia of the payload being significantly greater than that of the spacecraft (about 1.5:1 on EAC1).

(5) A stiffer payload structure as in EAC1 likely renders local reaction-wheel vibration isolation unnecessary. As mentioned, the contribution of hard-mounted reaction-wheels exported loads to dynamic wavefront errors are projected to be below 1 pm (1 $\sigma$) and preliminary simulations not reported here indicate other sources of errors such as the payload Attitude Determination System sensor noise will likely dominate the dynamics wavefront error budget.

(6) Perhaps counter-intuitively, a stiffer payload structure as in EAC1 allows reducing the electrical current drive bandwidth of the DFP voice-coil actuators despite the higher payload inertial attitude control bandwidth needed to achieve higher disturbance rejection in the presence of stiffer power cables. Uncontrolled, the back-emf in the DFP voice-coil actuators effectively acts as a viscous damper and is a source of vibration transmissibility in the presence of relative motion being the payload and the spacecraft: current drives limit that effect by negating the back-emf electrical current and the higher the back-emf rejection required, the higher the current drive bandwidth required. With higher stiffness cables, the vibration transmissibility due to the actuator back-emf becomes negligible as compared to the

transmissibility due to the cables and the benefit of countering the back-emf effects disappears. On EAC1, we opted to reduce the actuator current drive bandwidth from 160-Hz 0-dB cross-over on LUVOIR-B to 6-Hz 0-dB cross-over at the expense of back-emf rejection. That choice has the benefit of reducing the actuator current noise and therefore reducing the commensurate voice-coil actuation noise forces imparted to the payload: that in turn allowed us to reduce the dynamic wavefront errors due to the voice-coil actuator noise by a factor of at least 5. Being able to limit the voice-coil actuator current drive bandwidth to a frequency significantly below that of the primary mirror segment rigid-body modes results in significant reduction in the dynamic excitation of those modes.

(7) A stiffer payload structure allows the DFP design to close with sufficient control system stability margin. The interaction between the DFP control logic and the spacecraft flexible body dynamics increases as the interface cable stiffness increases because such increase leads to increased DFP relative-position and relative-attitude control bandwidth. The DFP control logic includes notch filters and gain stabilization filters to mitigate that interaction but for the DFP design to close, the payload structural modal frequencies are preferably a factor of 10 or more above the “rigid-body” modal frequencies of the coupled spacecraft-payload system due to the interface cables.

### *5.2 Payload Attitude Determination System is dominant source of dynamics line-of-sight and dynamic wavefront errors*

**Dynamic line-of-sight errors.** The Fine Guidance Sensors alone do not have enough resolution to achieve the 300-uarcsec (1 $\sigma$) line-of-sight stability goal. Within our design departure point, the payload attitude tip and tilt pointing errors are about 2.1 marcsec and 1.6 marcsec (1 $\sigma$), respectively, assuming a typical 3-marcsec (1 $\sigma$) FGS noise-equivalent-angle while operating on an 18-magnitude star at 20-Hz update rate.

Additional design margin is needed at this stage in the project to meet the line-of-sight objective. It would be desirable to increase the Fine Guidance Sensor resolution by a factor up to 10 to achieve the LOS stability goal. Alternatives include reducing the Payload inertial attitude control bandwidth currently set to 0.58-Hz 0-dB cross-over and stabilizing the line-of-sight at higher bandwidth using the Fast-Steering Mirror in the coronagraph optical path. There is a need to explore the design space combining all these options.

Assuming the FGS noise spectral density is uniform, the first option would require reducing the DFP Payload attitude control bandwidth by about 40x to 15-mHz: that approach is limited by the stiffness of the cable across the DFP interface and is undesirable as it forces the DFP system to operate at a bandwidth below the coupled spacecraft-payload-system natural frequency in the payload attitude degrees-of-freedom. Reducing the DFP attitude control bandwidth also translates into increased DFP range required to execute slews: we do not foresee that consideration as being necessarily a limitation because DFP has ample operational range margin to execute large angle slews; only 0.1-mm out of +/-10-mm operational range is required to execute slews in the current configuration.

The second option, namely the implementation of the Fast-Steering Mirror option explored in this study presumes the availability of a line-of-sight sensor in the coronagraph instrument with sufficient bandwidth and resolution for line-of-sight control. Our analyses indicate the line-of-sight control bandwidth would need to be about 2 Hz to achieve the line-of-sight stability objective with the current Fine Guidance Sensors, which implies a line-of-sight sensor update rate of about 20 Hz.

**Dynamic wavefront errors.** Now that we have a path to mitigate the impact of the spacecraft exported vibrations and the DFP actuation noise (both current drive noise and current command distortion in DAC conversion), the Payload Attitude Determination System dominates the dynamic wavefront errors above 5-Hz at about the 10:1 level. The ADS dynamic wavefront error contribution above 5 Hz is about 7 pm (1 $\sigma$), which may be acceptable depending on coronagraph sensitivity to random errors. Reducing the Payload inertial attitude control bandwidth could be explored as a mitigation path but as just discussed above such an approach has limitations.

### *5.3 DFP system properly manages impact of spacecraft exported vibrations and DFP-internal sources of errors on dynamic line-of-sight and dynamic wavefront errors*

As summarized in our line-of-sight and wavefront error budgets, our integrated modeling analyses indicate that the DFP system properly manages the impact of the spacecraft exported vibrations and DFP internal error sources.

Firstly, as explained in Section 5.1, that is in part due to the EAC1 payload structure being relatively stiff as compared to predecessor concepts LUVOIR-A and LUVOIR-B. On EAC1, we do not project needing vibration-isolation local to the reaction-wheels.

Secondly, we now have a viable path to mitigating the impact of the DFP actuator current-drive noise by tailoring the bandwidth of that drive.

### *5.4 Our OTA Active Alignment System sensor configuration analyses indicate a viable path exists to eliminate long distance metrology internal to the primary mirror*

We identified a combined edge-sensing and long-distance metrology configuration for sensing the OTA deformations, which eliminates the long-distance gauges internal to the primary mirror, and which has a good reconstructed-wavefront error (WEM<2) per JPL wavefront error metric (WEM) in Ref. 32. That configuration exploits flexibility in optical laser gauge placement for edge sensing not available with capacitive sensors (each sensor being approximately constrained to collocated orthogonal sense axis triad in that latter case). Our analyses indicate the placement flexibility offered by optical gauges is enough to overcome to a sufficient extent the observability challenges in sensing the primary mirror power mode. Absent that flexibility, one is led to using direct differential displacement measurements between the primary and the secondary mirror using long-distance gauges internal to the primary mirror as one's intuition suggests.

Such a configuration using optical gauges as edge sensors deserves further consideration as it eliminates the design dependency between the laser metrology and the primary mirror segment gap affecting coronagraph contrast while greatly simplifying OTA integration.

### *5.5 With conventional packaging methods, robustness to installation errors is a challenge for the long-distance metrology from the Primary Mirror to the Secondary Mirror to keep power losses manageable.*

Our analysis combining sensitivity to mechanical installation errors and link budget for the long-distance metrology indicates that the maximum allowable mechanical installation tolerances are challenging to meet while closing on link budget. Large power losses originate from propagation losses, mechanical misalignment-induced losses, or a combination of both depending on the beam diameter.

We envision the primary mirror segments and the secondary mirror will be brought into near alignment based on wavefront sensing so that the gauge mechanical installation errors will dominate the static errors and be the main driver on the gauge capture range (including cross input axis).

Our going-in position is to design the gauges to be robust to mechanical installation errors: in that approach the installation tolerances are handled strictly at the individual mirror build level with no adjustment required at the higher level of telescope integration (manually accessing gauges internal to the primary mirror, if any, for pointing adjustment at the higher level of telescope integration would be very challenging, and introducing remotely operable adjustment mechanisms would increase complexity and add mechanical interfaces prone to dimensional instabilities at the picometer level).

That strategy aims for (1) simplest gauge mechanical interface, (2) simplest integration for the observatory at the high level of integration, and (3) eliminating sources of dimensional instability in interfaces impacting picometer-class displacement sensing stability.

We are evaluating novel packaging methods to increase robustness to mechanical installation tolerances.

## 6 Conclusions and Future Work

We presented progress maturing four critical technologies for HWO, namely "Low-Vibration & Pointing Control Systems", "Telescope Sensing & Control", "Ultra-Stable Structures", and "Cryogenic Superconducting Detectors".

We presented detailed frequency-domain and time-domain integrated modeling analyses on EAC1 demonstrating that the Disturbance-Free-Payload system provides a path towards meeting the HWO telescope slew agility, inertial stabilization, and precision pointing needs while accommodating the harness required for large electrical power transfer across the vibration isolation system interface. We presented our approach for reducing the DFP voice-coil actuator current drive noise to mitigate DFP actuation disturbances should such mitigation become necessary in case the telescope structure is significantly more compliant and susceptible to residual exported vibrations than projected on EAC1. The implementation involves simple electrical drive circuit tuning. We presented our dynamic line-of-sight and dynamic wavefront bottoms ups error budgets supported by integrated structural-optical-control analyses showing that the spacecraft exported vibrations and DFP-induced disturbances are well-managed and no longer dominant sources of dynamic deformation errors. We highlighted the need for higher-resolution Fine Guidance Sensors and discussed the related payload attitude-determination-related trades being considered in the context of the DFP architecture to achieve the dynamic optical stability goals.

We reported the results of a laboratory experiment conducted by differencing the outputs from two Tracking Frequency Gauges on a common-path test-bed in air: the measurement instability achieved in that configuration is <3 pm over correlation times ranging anywhere from 3 msec to 2.8 hours. We presented sensor placement analysis results combining optical edge-sensing and long-distance metrology for the telescope Active Alignment System, which indicate that a viable path exists to eliminate long-distance metrology internal to the primary mirror, thereby eliminating the design dependency between the laser metrology and the primary mirror segment gap affecting coronagraph contrast while greatly simplifying OTA integration. We presented our progress on quantifying the robustness of heterodyne laser gauges to mechanical installation errors and concluded that conventional packaging and installation approaches lead to maximum allowable installation tolerances that are difficult to meet in the case of the long-distance metrology from the primary mirror to the secondary mirror.

Should structural damping augmentation become necessary to reduce the sensitivity of the optical telescope assembly to residual exported vibrations in case the telescope structure is significantly more compliant than projected on EAC1, we devised an approach for augmenting the structural damping in the suspension modes of the telescope primary and secondary mirrors, taking advantage of the existing picometer actuators used for positioning those elements. We implemented and analyzed that approach on EAC1 and achieved significant damping ranging from 4.2% to 9.5% of critical in all the mirror suspension modes.

We formulated and traded multiple cryogenic detector cooling options and selected a preferred option for packaging feasibility studies on the coronagraph instrument as a next step.

**Future work.** Our objectives are to continue maturing those four critical technologies for HWO and include the following near-term activities: (1) continue advancing and exercising integrated modeling tools to support HWO observatory architecture trades, end-to-end performance projections, and requirements decomposition, (2) incorporate OTA Active Alignment System into observatory integrated models and evaluate wavefront error rejection on EAC1, (3) assess impact of currently observed dynamic wavefront errors above 5 Hz on coronagraph contrast and develop recommendation on maximum allowable dynamic wavefront error, (4) define layout of cable harness bridging DFP interface; build and characterize representative cable sample to anchor integrated modeling activities and system performance projections, (5) quantify force noise of Tuned-Mass-Dampers under consideration for damping secondary tower bending modes and evaluate impact on OTA dynamic optical stability, (6) incorporate OTA structural damping augmentation in payload structural model and assess dynamic wavefront stability benefits, (7) design mounting interfaces between optical laser gauges and host mirrors conducive to picometer-class measurement stability, (8) explore innovative laser gauge internal packaging to increase robustness to mechanical installation alignment errors, and facilitate telescope integration, (9) evaluate packaging feasibility of selected cryogenic detector cooling option on coronagraph instrument.

*Acknowledgments*

This work was funded by the National Aeronautics and Space Administration under ROSES 2023 D.19 Critical Technologies for Large Telescopes (CT4LT).

*References*

1. Gaudi S., Seager S., Mennesson B., Kiessling A., and Warfield K., "The Habitable Exoplanet Observatory (HabEx)," in *Proc. SPIE: 11115, UV/Optical/IR Space Telescopes and Instruments: Innovative Technologies and Concepts IX, 11115-21*, San Diego, 2019.
2. Roberge A., Bolcar M. R., and France K., "Telling the story of life in the cosmos: the LUVOIR telescope concepts," in *Proc. SPIE 11115, UV/Optical/IR Space Telescopes and Instruments: Innovative Technologies and Concepts IX, 11115-23*, San Diego, 2019.
3. Feinberg L. et al. "Habitable Worlds Observatory’s Concept and Technology Maturation: Initial Feasibility and Trade Space Exploration", arXiv:2601.11803v3 [astro-ph.IM] 27 Jan 2026
4. Howe, Stark, and Sadleir, “The Scientific Impact of a Noiseless Energy-Resolving Detector for a Future Exoplanet-Imaging Mission”, https://arxiv.org/abs/2405.08883v1, 2024
5. Astrophysics Projects Division, “2022 Astrophysics Strategic Technology Gaps,” https://apd440.gsfc.nasa.gov/tech_gap-descriptions.html#tieronetop.
6. Pedreiro, N., “Spacecraft Architecture for Disturbance-Free Payload”, *Journal of Control, Guidance, and Dynamics*, Vol. 26, No. 5, 2003.
7. Pedreiro N., Carrier A., Lorell K., Roth D., Shelef G., Clappier R. and Gonzales M., "Disturbance-Free Payload concept demonstration," in *AIAA Guidance, Navigation and Control Conf. (AIAA-2002-5027)*, Monterey, 2002.
8. Pedreiro Nelson et al., “Agile Disturbance-Free Payload", *AIAA Guidance, Navigation, and Control Conference*, AIAA 2005-5876, San Francisco, CA, August 2005

9. Gonzales, Michael et al., “Unprecedented Vibration Isolation Demonstration Using the Disturbance-Free Payload Concept, *AIAA Guidance, Navigation, and Control Conference*, AIAA-2004-5247, Providence, RI, 2004.
10. Carrier, A.C. and et al., "Dynamic Wavefront and Line-of-Sight Performance Predictions for a 6-Meter Inscribed Diameter Habitable Worlds Observatory Segmented Telescope with Non-Contact Vibration Isolation and Pointing System," in *Towards the Habitable Worlds Observatory: Visionary Science and Transformational Technology*, Washington, D.C., 2025.
11. Carrier, A.C., Tajdaran, K., Jacoby, M.S., Nordt, A.A and Osborne, L., "Ultrastability Evaluation of Pathfinder Architecture for Habitable Worlds Observatory," in *UV/Optical/IR Space Telescopes and Instruments: Innovative Technologies and Concepts XII*, San Diego, CA, 2025.
12. National Aeronautics and Space Administration, *EAC-1 Architecture Configuration Report: Exploratory Architecture Cases Configuration Tracker,* Box Download, 2024.
13. Pueyo, L. and e. al., "The LUVOIR Extreme Coronagraph for Living Planetary Systems (ECLIPS) I: searching and characterizing exoplanetary gems," *SPIE Techniques and Instrumentation for Detection of Exoplanets IX,* vol. Vol. 11117, 2019.
14. Space Telescope Science Institute, "WFC3 Instrument Handbook: UVIS Exposure and Readout," [Online]. Available: https://hst-docs.stsci.edu/wfc3ihb/chapter-6-uvis-imaging-with-wfc3/6-7-uvis-exposure-and-readout. [Accessed October 2025].
15. National Aeronautics and Space Administration, "LUVOIR Final Report," https://asd.gsfc.nasa.gov/luvoir/reports/LUVOIR_FinalReport_2019-08-26.pdf, 2019.
16. Northrop Grumman, "SSIRU™ Family of Products," 2021. [Online]. Available: https://www.northropgrumman.com/what-we-do/mission-solutions/assured-navigation/scalable-space-inertial-reference-unit. [Accessed Feb 2026].
17. Freesland, Doug et al., “GOES-R Dual Isolation”, *American Astronautical Society, Guidance & Control Conference* AAS 15-061, 2015.
18. Carrier, Alain, “Modeling of a Segmented Telescope Habitable Worlds Observatory”, Towards starlight suppression for the Habitable Worlds Observatory workshop, August 2023.
19. National Academies of Sciences, Engineering, and Medicine 2021. *Pathways to Discovery in Astronomy and Astrophysics for the 2020s.* Washington, DC: The National Academies Press. https://doi.org/10.17226/26141.
20. Ames, Lawrence L., Barrett, Robert, Bell, Raymond Bell Jr., Dries, Lawrence J., Dutta, Kalyan, Halverson, Peter G., Holmes, Buck, Kvamme, Eric T., Leary, David F., Perkins, Patrick, Scott, Mark, Van Eck, Timothy E., Zhao, Feng, “SIM external metrology beam launcher (QP) development,” *Proc. SPIE 4852, Interferometry in Space*, (26 February 2003).

21. Ames, Lawrence L., Barrett, Stephanie D., Calhoon, Stuart J., Kvamme, Eric T., Mason, James E., Oseas, Jeffrey M., Pryor, Mark, Schaechter, David B., Stubbs, David M., “Space Interferometry Mission starlight and metrology subsystems,” *Proc. SPIE 4852, Interferometry in Space*, (26 February 2003).
22. Bell, R.,“Robust heterodyne interferometer optical gauge.” Patent US Pat. 6947621, 2002.
23. Bell, R., “Waveguide-based optical interferometer.” Patent US Pat. 7003186, 2003.
24. Bell, R., “Beam masking to reduce cyclic error in beam launcher of interferometer.” Patent US Pat. 6922249, 2002.
25. Horowitz, Luke, Mason, James, Hilby, Timothy, Rother, Aaron, and Nordt, Alison, “A picometer class displacement metrology system using photonic integrated circuit,” *Proc. SPIE 11816, Optomechanics and Optical Alignment*, 1181604 (1 August 2021).
26. Wirth, Jacob, Mason, James, and Nordt, Alison, “Progress in demonstrating picometer class laser metrology using photonics integrated gauges,” *Proc. SPIE 12180, Space Telescopes and Instrumentation 2022*: Optical, Infrared, and Millimeter Wave, 121805X (27 August 2022).
27. Reasenberg, R.D., Babcock, R.W., Murison, M.A., Noecker, M.C., Phillips, J.D., Schumaker, B.L., Ulvestad, J.S., McKinley, W., Zielinski, R.J., and Lillie, C.F., "POINTS: High Astrometric Capacity at Modest Cost *via* Focused Design," *SPIE 2807*, pp 32-50, 1996.
28. Phillips, J.D. and Reasenberg, R.D., “Tracking frequency laser distance gauge,” *Rev. Sci. Instrum*. **76** (2005) 064501.
29. Thapa, R., Phillips, J.D., Rocco, E. and Reasenberg, R.D., “Sub-Picometer Length Measurement Using Semiconductor Laser Tracking Frequency Gauge,” *Opt. Lett.* **36** (2011) 3759.
30. Kaplan, D.M., Roberts, T.J., Phillips, J.D., and Reasenberg, R.D., “Improved Performance Of Semiconductor Laser Tracking Frequency Gauge,” *JINST* **13** (2018) P03008.
31. Reasenberg, R.D., "Filtering with Perfectly Correlated Measurement Noise," *AIAA Journal*, **10**, 942, 1972.
32. Redding, David, Basinger, Scott, Bikkannavar, Siddarayappa, Dube, Brandon, Kee, Andrew, Lou, John, Nissly, Carl, Ohara, Catherine, Poon, Philip, Sidick, Erkin, Tesch, Jonathan, Troy, Mitchell, "Wavefront sensing and control for a future Habitable Worlds Observatory," *Proc. SPIE 13092, Space Telescopes and Instrumentation 2024*: *Optical, Infrared, and Millimeter Wave*, 130921P (23 August 2024); https://doi.org/10.1117/12.3020583
33. Maly, J.R. and Johnson, C.D. “Co-cured Viscoelastic Composites,” *Smart Structures and Materials: Passive Damping and Isolation*, Feb. 1996, San Diego, CA.

34. Hsu, S., Mor, M., Stirling, B., and Glaese, R. "Reduction of Dynamic Response of a Wind Tunnel Mount Using Co-Cured Composite and Viscoelastic Materials," *48th AIAA Aerospace Sciences Meeting, Jan. 2010, Orlando, FL*. AIAA 2010-1308.
35. Maly, J., Napolitano, K., "A Magnetic Tuned-Mass Damper for Buffet-Induced Airfoil Vibration," *Damping '93*, San Francisco, California.
36. Maly, J., Yingling, A., Griffin, S., Agrawal, B., Cobb, R., Chambers, T., "Vibration Damping for the Segmented Mirror Telescope," *SPIE Astronomical Telescopes and Instrumentation, 2012*, Amsterdam, Netherlands.
37. Maly, J.R., Keas, P.J., and Glaese, R.M. "Damping SOFIA: passive and active damping for the Stratospheric Observatory for Infrared Astronomy," *Proc. SPIE Vol 4331 Smart Structures and Materials 2001: Damping and Isolation,* July 2001, Newport Beach, CA, pp. 60-71.
38. Keas, P.J., Dunham, E. et al, "Active damping of the SOFIA Telescope assembly," *Proc. SPIE Vol 8444 Ground-based and Airborne Telescopes IV, 2012*, Amsterdam, Netherlands.
39. Anderson, E.H., Holcomb, D. et al "Integrated Electromechanical Devices for Active Control of Vibration and Sound," *International Mechanical Engineering Congress and Exposition, Nov. 1997*, Dallas, TX.
40. Bales, G.L., Glaese, R.M. et al "Active Damping and Vibration Control for Aircraft Fin and Appendage Structures," *AIAA Aerospace Sciences Meeting, Jan. 2006*, Reno, NV.
41. Irwin and Hilton, Transition-Edge Sensors, 63–150. Springer Berlin Heidelberg, Berlin, Heidelberg (2005). https://link.springer.com/chapter/10.1007/10933596_3
42. Zobrist, Clay, Coiffaard, Daal, Swimmer, Day, and Mazin, *Physical Review Letters*, Volume 129, Issue 1, article id.017701, July 2022, https://ui.adsabs.harvard.edu/abs/2022PhRvL.129a7701Z/abstract
43. Tuttle, James et al., "Development of a space-flight ADR providing continuous cooling at 50 mK with heat rejection at 10 K", *IOP Conf. Series: Materials Science and Engineering* 278 (2017) 012009 https://doi.org/10.1088/1757-899X/278/1/012009.
44. Naes, Wu, Cannon, Lloyd, Schick, "WISE solid hydrogen cryostat design overview", *Proceedings Volume 5904, Cryogenic Optical Systems and Instruments XI*; 590413 (2005) https://doi.org/10.1117/12.619142.
45. Schick and Bell, "Performance of the Spirit III cryogenic system", *Proceedings Volume 3122, Infrared Spaceborne Remote Sensing V*; (1997) https://doi.org/10.1117/12.279007.
46. Breedlove et al., "Testing of a Two-Stage 10 K Turbo-Brayton Cryocooler for Space Applications", *Cryocoolers 18*, pp 445-452, 2014.
47. Zagarola, M., Creare LLC, private communication.

48. Vila, B. et al. "JWST Fine Guidance Sensor Commissioning and Performance During Operations", *SpaceOps-2025, 18$^{th}$ International Conference on Space Operations*, Montreal, Canada, May 2025

**Dr. Alain Carrier** is a Senior Fellow research scientist at Lockheed Martin Advanced Technology Center. He received his doctorate degree in Aeronautics and Astronautics from Stanford University in 1990. His expertise is in design, dynamics modeling, and robust control synthesis of precision mechanisms for astronomical and earth sensing instruments. As Principal Investigator for the past 35 years, he led advanced technology development in diverse areas of vibration isolation and control, optical-precision pointing, active mirror mechanisms, inertial navigation systems, gradiometers, dynamics modeling and uncertainty quantification, system identification, numerical optimization algorithms, smart actuators, earth observation instruments, space interferometry, next generation space telescopes. His current research interests include modeling-and-control of large, ultra-stable, segmented telescopes, and quantum inertial sensing for inertial navigation. He is a member of SPIE.

Biographies and photographs for the other authors are not available.

## Caption List

**Fig. 1** (Credit NASA): Exploratory Analytical Case 1 Overview.

**Fig. 2** DFP Demonstrated Superior Levels of Vibration Isolation on 3D Emulators Relevant to HWO Replicating the Dynamics of Large Observatories at Reduced Scale.

**Fig. 3** The pure DFP control system configuration.

**Fig. 4** Current Noise Density and Back EMF Attenuation of Simulated Circuits.

**Table 1** Simulation Results for Voice Coil Drive Circuits.

**Table 2** Data Rate and Power Estimates for Payload Components in EAC-1.

**Fig. 5** DFP control logic includes cable stiffness cancellation option and associated built-in test capability for on-orbit characterization.

**Fig. 6** The components which comprise Lockheed Martin's heterodyne laser metrology system**.**

**Fig. 7** (Left) PIC waveguide layout. (Right) Silicon nitride PIC.

**Fig. 8** Allan deviation of PIC internal measurement errors.

**Fig. 9** Opto-electronic design for TFG tests at IIT.

**Fig. 10** Allan deviation vs. averaging time of a recent TFG test run in optical cavity at IIT.

**Fig. 11** Left: Optical Telescope Assembly with a sample laser metrology truss for one primary segment and the aft metering structure. Right: Edge sensor location and measurement directions for EAC-1 sensors.

**Fig. 12** Wavefront error multiplier (WEM) for various external metrology configurations including an alternative configuration with LDGs only at the outside perimeter of the primary mirror. Green cases represent a WEM <2 and red a WEM>10.9.

**Fig. 13** Alternative edge sensing configuration using 6 pairs of crossed laser metrology gauges.

**Fig. 14** WEM using alternative edge sensing configuration as a function of $\theta$, and $\gamma$. Left: using all LDG, Right: using perimeter only LDG.

**Fig. 15** Open and closed-loop response plots showing benefit of active tuned mass damping for secondary mirror support structure.

**Fig. 16** Open and closed-loop response plots showing benefit of active damping control for picometer positioning system.

**Table 3** Kepner Tregoe Analysis of cryocooler configuration options.

**Table 4** Kepner Tregoe Analysis Scoring rationale.

**Fig. 17** Description of Recommended Crygenic Detector Cooling System Configuration.

**Fig. 18** Overview of Payload and Spacecraft Structural Dynamics Models.

**Table 5** Design Departure Point Configuration.

**Table 6** Payload Attitude Determination System Configuration.

**Fig. 19** Rigid-body and flexible-body spacecraft disturbance transmissibility.

**Fig. 20** Transmissibility from Spacecraft Vibration to Dynamic Line Of Sight Error.

**Fig. 21** Transmissibility from Spacecraft External Loads to Dynamic Wavefront Error.

**Fig. 22** Transmissibility from Spacecraft Reaction-Wheel Exported Loads to Dynamic Wavefront Error.

**Fig. 23** EAC1 Steady-State Dynamic Optical Stability Performance.

**Fig. 24** EAC1 Steady-State Dynamic Wavefront Error Performance.

**Fig. 25** Payload Attitude Determination System Performance: Payload Attitude Reconstruction Error.

**Fig. 26** Steady-State Payload Attitude Control Error.

**Fig. 27** Coordinated Large Angle Slew with Spacecraft and Payload Flexible Body Dynamics.

**Fig. 28** Past Recentering Maneuver, Sensing Range Required of Relative Position Sensors to Execute Slew is Less Than 0.1 mm Out of +/-12-mm Available Range

**Fig. 29** Past Recentering Maneuver, Winding Current Required of Non-Contact Voice-Coil Actuators to Execute Slew is Less Than 30 mA Out of +/-2 A Available Range.

**Fig. 30** EAC1 Dynamic Optical Stability Performance Past End of Slew Achieved With DFP System.

**Fig. 31** EAC1 Dynamic Wavefront Error Performance Past End of Slew Achieved With DFP System.

**Table 7** Dynamic Line-Of-Sight Error Budget.

**Table 8** Dynamic Wavefront Error Budget.